Chromatin accessibility dynamics of neurogenic niche cells reveal a reversible decline in neural stem cell migration during aging

Robin W. Yeo[1], Olivia Y. Zhou[1,2,3], Brian Zhong[4], Mahfuza Sharmin[1], Tyson J. Ruetz[1], Anshul Kundaje[1,5], Alexander R. Dunn[4], Anne Brunet[1,6,*]

Affiliations

[1] Department of Genetics, Stanford University, Stanford, CA, USA

[2] Stanford Biophysics Program, Stanford University, Stanford, CA, USA

[3] Stanford Medical Scientist Training Program, Stanford University, Stanford, CA, USA

[4] Department of Chemical Engineering, Stanford University, Stanford, CA, USA

[5] Department of Computer Science, Stanford University, Stanford, CA, USA

[6] Glenn Laboratories for the Biology of Aging, Stanford University, Stanford, CA, USA

[*]email: abrunet1@stanford.edu

Abstract

Aging is accompanied by a deterioration in the regenerative and repair potential of stem cell regions in the brain. However, the mechanisms underlying this decline are largely unknown. Here we profile the chromatin landscape of five different cell types freshly isolated from the subventricular zone neurogenic niche of young and old mice. We find that chromatin states exhibit distinct changes with aging in different cell types. Notably, the chromatin of quiescent neural stem cells (NSCs) becomes more repressed with age whereas that of proliferative, activated NSCs becomes more open. Surprisingly, these opposing age-related chromatin changes involve cell adhesion and migration pathways. We experimentally validate that quiescent and activated NSCs exhibit opposite migratory deficits during aging. Quiescent NSCs become more migratory during aging, whereas activated NSCs and progeny become less migratory and less able to mobilize out of the niche *in vivo* during aging. The cellular mechanism by which aging impairs the migration of activated NSCs and progeny involves increased occurrence of force-producing focal adhesions. Inhibiting the cytoskeletal-regulating kinase ROCK in old activated NSCs and progenitors eliminates cell adhesive forces and boosts migration speed, reverting these cells to a more youthful migratory state. Our work has important implications for restoring the migratory potential of NSCs during aging and brain injury.

47 **Main text**

48

49 The adult brain contains regenerative neural stem cell (NSC) niches, with progenitors that
50 can migrate to distal brain regions to generate new neurons and glial cells[1]. The regenerative
51 potential of stem cell regions in the brain declines with age, and this is accompanied by a
52 corresponding deterioration in aspects of sensory and cognitive function and in repair ability[2-6].
53 The subventricular zone (SVZ) neurogenic niche provides an excellent paradigm for studying
54 NSC function and migration during aging. In this niche, quiescent NSCs line the ventricular
55 wall[7-9]. Quiescent NSCs can activate and in turn generate progenitors and neuroblasts that
56 migrate towards the olfactory bulb to produce new neurons[10]. Subventricular zone NSC progeny
57 also migrate to sites of injury to mitigate damage by generating new neurons[11] and astrocytes[12].
58 Both the regenerative potential and repair abilities of the SVZ neurogenic region deteriorate with
59 age[13-16]. But the mechanisms underlying regenerative decline during aging – and how defects in
60 migratory potential might be involved – remain largely unknown.

61

62 Epigenomic changes that affect chromatin states play an important role in the regulation
63 of cell fate[17] and aging[18]. So far, however, epigenomic studies of NSCs have been limited to
64 whole tissues *in vivo*[19] or to culture systems[20-22], and age-dependent epigenomic changes in
65 different cell types of the neurogenic niche *in vivo* are unknown. While several cellular and
66 signaling defects in neurogenic niches during aging have been uncovered by transcriptomic
67 studies[23-26], changes to the chromatin landscape of NSCs could have a longer-lasting impact on
68 the progeny and reveal features of aging that were previously undetected. Identifying chromatin

69 changes in different cell types from the neurogenic niche during aging could help reverse age-
70 dependent defects in regeneration and repair and counter brain aging.
71
72 **The chromatin landscape of five cell types in the SVZ neurogenic region reveals opposing**
73 **chromatin changes with age in quiescent and activated NSCs involving cell adhesion and**
74 **migration pathways**
75 To determine the impact of aging on the chromatin landscape of cells in the neurogenic
76 niche *in vivo*, we generated chromatin accessibility profiles from five distinct cell types freshly
77 isolated from the subventricular zone (SVZ) neurogenic niche of young and old mice. To this
78 end, we aged cohorts of transgenic mice expressing green fluorescent protein driven by the
79 promoter for glial fibrillary acidic protein (GFAP-GFP), which allows the isolation of different
80 cell types by fluorescent activated cell sorting (FACS)[27]. The SVZ neurogenic regions of young
81 (3-5 months old) and old (20-24 months old) GFAP-GFP mice were micro-dissected, and five
82 cell populations from this neurogenic niche were freshly isolated by FACS[27,28] – endothelial
83 cells, astrocytes, quiescent NSCs (qNSCs), activated NSCs (aNSCs), and neural progenitor cells
84 (NPCs) (Fig. 1a, Extended Data Fig. 1a). To assess chromatin accessibility genome-wide on
85 these rare cell populations (~100-1000 cells per individual), we used ATAC-seq[29-33] (Fig. 1a).
86 We verified that ATAC-seq libraries across all conditions exhibited stereotypical 147-bp
87 nucleosome periodicity (Extended Data Fig. 1b) and strong enrichment of accessibility around
88 transcription start sites (TSSs) (Extended Data Fig. 1c). Principal component analysis (PCA)
89 (Fig. 1b) and hierarchical clustering (Extended Data Fig. 2a) on accessible chromatin peaks
90 easily separated endothelial cells from other brain cells, and quiescent cells (astrocytes and
91 qNSCs) from activated ones (aNSCs and NPCs). The locus for *Ascl1*, a neural lineage gene

92 involved in NSC activation[34], shows accessible chromatin peaks in all neural cell types but not in
93 endothelial cells, and several chromatin peaks are higher in aNSCs and NPCs than in qNSCs and
94 astrocytes (Fig. 1c), consistent with *Ascl1* mRNA expression (Extended Data Fig. 2b).
95 Additionally, chromatin accessibility at promoters positively correlated with mRNA expression
96 genome-wide (Extended Data Fig. 2c). Thus, these genome-wide chromatin accessibility datasets
97 are of high quality and represent a useful resource for studying age-related chromatin changes in
98 5 different cell types freshly isolated from the regenerative SVZ neurogenic niche.
99
100 Chromatin accessibility allowed separation of quiescent and activated NSCs by age (Fig.
101 1d for PC3, Extended Data Fig. 3a for PC2). In line with transcriptional studies[25,26,28], more
102 chromatin peaks change with age in qNSCs (7,354) than in aNSCs (2,311) (FDR < 0.05)
103 (Extended Data Fig. 3b, Supplementary Table 3). But interestingly, chromatin accessibility could
104 separate young and old aNSCs whereas gene expression could not (Fig. 1d), suggesting that
105 analyzing chromatin states may reveal new genes and pathways that had not been previously
106 implicated in NSC aging. As expected, chromatin peaks were located either at promoters or at
107 intronic and distal regions, which are known to contain non-coding regulatory elements such as
108 enhancers (Fig. 1e). Performing PCA exclusively on distal and intronic chromatin peaks
109 (putative enhancer-containing sites) was sufficient to separate NSCs based on age (Fig. 1f,
110 Extended Data Fig. 3c,d), whereas chromatin accessibility at promoter regions alone was not
111 (Extended Data Fig. 3e), suggesting that non-coding regulatory elements may be particularly
112 sensitive to changes during aging.
113

114 Surprisingly, aging had opposing effects on chromatin accessibility dynamics in qNSCs
115 and aNSCs. While most dynamic peaks in activated cells open with age, most dynamic peaks in
116 quiescent cells closed with age (Fig. 1g). Likewise, the genome-wide chromatin landscape of old
117 aNSCs contained more accessible chromatin peaks but less nucleosomes than that of young
118 aNSCs while the opposite was true for qNSCs (Extended Data Fig. 3f,g). Chromatin peaks that
119 dynamically change with age in qNSCs and aNSCs were almost entirely distal or intronic
120 (Extended data Fig. 3h, Supplementary Table 3). Thus, the chromatin of activated NSCs
121 becomes more permissive with age while the chromatin of their quiescent counterparts becomes
122 more repressed, and these changes occur in putative enhancer-containing regions.
123
124 Gene Ontology (GO) biological pathway enrichment on qNSC and aNSC genes with
125 regulatory regions that exhibited differential accessibility with age revealed cell adhesion and
126 migration as defining hallmarks of aging in both qNSCs and aNSCs. Old qNSCs had decreased
127 chromatin accessibility at pathways involved in promoting cell adhesion and inhibiting cell
128 migration ("response to forskolin", "cAMP-mediated signaling", "negative regulation of cell
129 motility", "cell-cell adhesion (plasma membrane)" (Fig. 1h, Supplementary Table 4).
130 Conversely, old aNSCs had increased chromatin accessibility at regulatory regions of genes
131 associated with increased cell adhesion ("cell-cell adhesion (cadherins)", "homophilic cell
132 adhesion (plasma membrane)", "adherens junction organization") compared to young aNSCs
133 (Fig. 1i, Supplementary Table 4). Consistently, young qNSCs and old aNSCs were grouped
134 together based largely on cell adhesion pathways along the principal component 2 (PC2) axis
135 (Extended data Fig. 4a, Supplementary Table 6,7). These opposing changes in qNSCs and
136 aNSCs during aging are unlikely to be solely due to increased heterogeneity of cell populations

137 with age because they were also observed in scRNA-seq (Fig. 2d below) and *in vivo* brain
138 sections (Fig. 3a-c below). Thus, aging has opposing effects on the global chromatin landscape
139 of qNSCs and aNSCs, including changes to chromatin accessibility in regulatory regions
140 involved in cell adhesion and migration.
141

142 **The opposing chromatin changes in old quiescent and activated NSCs with aging are**
143 **associated with functional defects in cell adhesion and migration**

144 We next examined age-dependent changes in chromatin accessibility and mRNA
145 expression of specific genes involved in cell adhesion and migration. Old qNSCs freshly isolated
146 from the brain showed reduced chromatin accessibility at regulatory regions of cell adhesion
147 genes, including *Cdhr3* (Cadherin Related Family Member 3) (Fig. 2a, b). In contrast, old aNSCs
148 exhibit increased chromatin accessibility at regulatory regions of cell adhesion genes, including
149 cadherins and *Pcdh18* (proto-cadherin 18) (Fig. 2a, b), overlapping with a number of adhesion
150 genes enriched in young qNSCs (Extended Data Fig. 4b). Old NPCs also exhibit increased
151 accessibility at adhesion pathways with age (Extended Data Fig. 4c, Supplementary Table 4),
152 indicating that some of these age-related changes are preserved in downstream progeny. Motif
153 enrichment analysis using a deep learning approach (DeepLift[35] and TF-MoDISCO[36,37], see
154 Methods) identified the motifs for NFI transcription factors NFIB and NFIC among the most
155 enriched within the differentially accessible chromatin regions that close with age in qNSCs and
156 open with age in aNSCs freshly isolated from the brain (Fig. 2c). The NFI transcription factor
157 family regulates cellular adhesion pathways in NSCs[20], and NFI isoforms affect cellular
158 migration[38]. Hence, open chromatin dynamically changes in an opposing manner at regulatory
159 regions of genes that contain binding sites for a key cell adhesion transcription factor.

160 Importantly, re-analysis of single-cell RNA-seq from the young and old neurogenic SVZ niche[25]
161 showed that old qNSCs/astrocytes have decreased expression of genes involved in cell adhesion
162 pathways compared to their young counterparts while old aNSCs/NPCs exhibit increased
163 expression of cell adhesion genes compared to their young counterparts (Fig. 2d). Furthermore,
164 changes in NSC adhesion during aging are unlikely to be explained solely by differences in cell
165 cycle status, as cell adhesion and cell cycle signatures could be uncoupled at the single cell level
166 (Extended Data Fig. 5). Thus, in quiescent and activated NSCs, aging leads to opposing changes
167 in the chromatin accessibility and mRNA expression of genes involved in cell adhesion.
168
169 Our chromatin dynamics results predict that the adhesive properties of NSCs change with
170 age. To directly test if aging functionally impacts the migratory properties of NSCs in an
171 opposing manner, we used a culture system for quiescent NSCs and proliferative NSCs (a mix of
172 aNSCs/NPCs)[20,28,39-41](Fig. 2e,f). We verified that the chromatin landscape of cultured NSCs was
173 similar to that of freshly isolated NSCs (Extended Data Fig. 6a-e, Supplementary Tables 3,4,5),
174 notably in its age-related changes to cell adhesion and migration pathways (Fig. 2g,h). To
175 quantify NSC migration in culture, we performed continuous live-cell imaging of cultured NSCs
176 over the course of 20 hours (Fig. 2i). Interestingly, old qNSCs were slightly more migratory (less
177 adhesive) compared to their young counterparts (mean velocities: young (2.998 μm/hr) vs. old
178 (3.465 μm/hr)) (Fig. 2j, Extended Data Fig 6f), whereas old aNSCs/NPCs were less migratory
179 (more adhesive) compared to their young counterparts (mean velocities: young (13.618 μm/hr)
180 vs. old (9.928 μm/hr)) (Fig. 2k, Extended Data Fig. 6g). Quantifying the migration of cultured
181 aNSCs/NPCs through Matrigel, a hydrogel composed of extracellular matrix (ECM) proteins,
182 confirmed that aNSCs/NPCs cultured from old brains exhibit impaired migration through ECM

183 compared to their young counterparts (Fig. 2l,m). Hence, aging has opposing effects on the
184 adhesive and migratory properties of quiescent and activated NSCs in culture, with qNSCs
185 becoming less adhesive and aNSCs/NPCs becoming more adhesive in old age.
186
187 **Age-dependent cell adhesion and migration defects of quiescent and activated NSCs and**
188 **progenitors *in vivo***
189 Quiescent NSCs line the ventricles and can become activated (aNSCs) to give rise to
190 neural progenitors (NPCs) and neuroblasts that migrate along the rostral migratory stream (RMS)
191 to the olfactory bulb (OB)[10,42,43]. While neuroblast migration has begun to be examined in older
192 animals[44-47], the adhesive and migratory properties of quiescent and activated NSCs and their
193 progenitors *in vivo* during aging remain largely unstudied. As adhesion to the niche plays a key
194 role in regulating NSC stemness and function[48], we assessed quiescent and activated NSC
195 localization *in vivo* by immunostaining of coronal brain sections from young and old individuals
196 (Fig. 3a,b). In old brains, quiescent NSCs and niche astrocytes (GFAP+/Ki67-) were located
197 further away from the ventricle, while activated NSCs (GFAP+/Ki67+) were located closer to
198 the ventricle than in young brains (Fig. 3c). Together with functional data from cultured NSCs
199 (Fig. 2), these results suggest that quiescent NSCs become less adherent to the ventricle while
200 activated NSCs become more adherent during aging.
201
202 We next probed the migratory properties of activated NSCs and progeny during aging *in*
203 *vivo*. To this end, we injected young and old mice with the thymidine analog 5-Ethynyl-2'-
204 deoxyuridine (EdU), which incorporates into the DNA of replicating cells, to label and trace
205 activated NSCs and their progeny. We assessed the number of EdU-positive (EdU+) cells in the

206 SVZ niche, the migration route (RMS), and destination (OB), at a short (4 hours), mid- (2 days),
207 or long (7 days) time point after EdU injection (Fig. 3d-f, Extended Data Fig. 7a). While
208 successive rounds of cell division can dilute EdU signal[49], nucleoside analogs have been used to
209 study SVZ neurogenesis in longer time frames (31 days)[16]. In young individuals, EdU+ cells
210 were numerous in the niche and along the RMS 4 hours after EdU injection (Fig. 3g,h). After 7
211 days, young animals showed a dramatic reduction of EdU+ cells in the niche and RMS, and a
212 corresponding increase in EdU+ cells in the OB, consistent with mobilization out of the niche
213 and clearance from the RMS towards the OB (Fig. 3g-i). In old individuals, EdU+ cells were less
214 numerous, as expected[15,16,50,51] (Fig. 3f, Extended Data Fig. 7b), but they neither significantly
215 decreased in the SVZ niche after 7 days (Fig. 3j) nor increased in the OB after 7 days (Fig. 3l). In
216 the aged neurogenic niche, old EdU+ aNSCs/NPCs and neuroblasts (Extended Data Fig. 7c)
217 were located closer to the ventricle, after a 4 hour EdU pulse, than their young counterparts (Fig.
218 3m-o). These observations are consistent with an inability of old aNSCs and progeny to mobilize
219 out of the old neurogenic niche. We did observe some clearance of EdU+ cells through the old
220 RMS after 7 days (Fig. 3k), suggesting that old neuroblasts retain some motility in the RMS[44],
221 but migrate more slowly than young neuroblasts. Thus, aging impairs the tight localization of
222 quiescent NSCs to the ventricles and decreases the migratory ability of old aNSCs and
223 downstream progeny (NPCs and neuroblasts) to their distal destination *in vivo*.
224
225 **Aging increases the occurrence of force-producing focal adhesions in aNSCs/NPCs**
226 We assessed the cellular mechanisms underlying the decrease in migratory properties of
227 aNSCs and progenitors, and their increased cell adhesion, during aging. Adhesion of cells to the
228 extracellular matrix (ECM) primarily involves integrin-mediated linkage between ECM and actin

229 cytoskeleton (Fig. 4a). We first used immunofluorescence staining to visualize the F-actin
230 cytoskeleton and quantify bundled actin, which contributes to cellular adhesion through the
231 formation of stress fibers, lamellipodia, and filopodia[52,53]. Activated NSCs/NPCs cultured from
232 old brains exhibited increased staining for bundled actin compared to young counterparts (Fig.
233 4b,c). Thus, the age-related migratory deficit of old cultured aNSCs/NPCs is accompanied by
234 increased cytoskeletal assembly, which is necessary for integrin-based adhesion to the ECM.
235
236 To directly visualize the mechanical forces imparted by aNSCs/NPCs interacting with
237 their substrate, we next leveraged Förster resonance energy transfer (FRET)-based molecular
238 tension sensors (Fig. 4a)[54,55]. Molecular tension sensors reveal forces exerted by aNSCs/NPCs on
239 surfaces coated with synthetic arginine-glycine-aspartate (RGD) peptides known to bind
240 integrins and mediate adhesion[55], with higher forces corresponding to a reduction in FRET (Fig.
241 4a). FRET measurements revealed that aNSCs/NPCs primarily exert force though distinct focal
242 adhesion complexes at their periphery (Fig. 4d). Consistently, bundled actin also aggregated
243 peripherally in aNSCs/NPCs (Extended Data Fig. 8a). We quantified the adhesive force patterns
244 for young and old cultured aNSCs/NPCs and found that their focal adhesion profiles were
245 bimodal, with a population of cells exhibiting force-producing focal adhesions and a population
246 with no force-producing focal adhesions (Fig. 4e,f). While aging does not significantly affect
247 individual focal adhesion strength or area (Fig. 4e, Extended Data Fig. 8b), old aNSCs/NPCs
248 were more likely to exhibit force-producing adhesions than young aNSCs/NPCs (Fig. 4f,
249 Extended Data Fig. 8c-e) (P=0.0327, combined Fisher's exact test). Specifically, old
250 aNSCs/NPCs were much more likely than young aNSCs/NPCs to exhibit force-producing
251 adhesions when in contact with other cells (Extended Data Fig. 8f,g). Thus, a higher prevalence

252 of force-producing adhesions in old aNSCs/NPCs likely contributes to the functional
253 deterioration in the migration of activated NSCs and their progeny in the aged brain.
254
255 **Inhibition of ROCK boosts migration speed and eliminates focal adhesions in aNSCs/NPCs**
256 **from aged brains**
257 To identify a molecular target to modulate and potentially reverse the age-related
258 migratory deficit of old activated NSCs and progenitors, we used Ingenuity Pathway Analysis
259 (IPA) to enrich for signaling pathways associated with the chromatin accessibility changes seen
260 in old aNSCs/NPCs. Pathway enrichment by IPA revealed a number of signaling pathways
261 including some involved in cell adhesion (Fig. 5a, Supplementary Table 8), consistent with our
262 GO analysis (see Fig. 1i). The most enriched pathway in this cluster was Gα 12/13 signaling
263 (Fig. 5a), which regulates cell adhesion in part via Rho and Rho-associated protein kinase
264 (ROCK)[56,57] (Fig. 5b). ROCK plays a major role in regulating the actin cytoskeleton and cell
265 adhesion (among other phenotypes)[58], and it could serve as a molecular target to reverse the age-
266 dependent decline in aNSC/NPC migration.
267
268 To determine if the migratory properties of old aNSCs and their progenitors could be
269 ameliorated via modulation of the ROCK pathway, we targeted ROCK with the small molecule
270 inhibitor Y-27632[59-66] in cultured aNSCs/NPCs. Quantification of force patterns on RGD
271 molecular tension sensors (Fig. 5c) revealed that treating old aNSCs/NPCs with the ROCK
272 inhibitor Y-27632 eliminated force-producing focal adhesions (Fig. 5d,e). Consistently,
273 inhibiting ROCK in old aNSCs/NPCs also resulted in decreased staining for bundled actin (Fig.
274 5f,g). ROCK inhibition resulted in improved migration speed in both young and old

275 aNSCs/NPCs (mean velocities: young (13.618 μm/hr) vs. young + Y-27632 (20.201 μm/hr); old
276 (9.928 μm/hr) vs. old + Y-27632 (21.691 μm/hr)) (Fig. 5h,i, Extended Data Fig. 8h,
277 Supplementary Videos 1,2). Furthermore, inhibiting ROCK rescued the age-related decline in
278 old aNSC/NPC migration through ECM (Fig. 5j). Together, these data indicate that inhibition of
279 the ROCK pathway could ameliorate the age-related migratory deficit of old aNSCs and
280 progenitors for neurogenesis and repair targets.
281
282 **Discussion**
283 Our study is the first to identify age-related genome-wide changes to the global
284 chromatin landscape of quiescent and activated NSCs freshly isolated from the adult SVZ
285 neurogenic niche. This analysis reveals that aging has opposing effects on the opening and
286 closing of dynamic chromatin regions in quiescent and activated NSCs, with many of these
287 changes affecting adhesion and migration pathways. Our study also shows for the first time that
288 old activated NSCs and progenitors exhibit impaired migration, and that ROCK inhibition boosts
289 the migratory ability of these cells in culture partly by decreasing the formation of force-
290 producing adhesions. This work could uncover new strategies to restore age-dependent defects in
291 regeneration and repair by targeting adhesive and migratory changes with age.
292
293 The chromatin landscape of quiescent NSCs becomes less open with age whereas that of
294 activated NSCs becomes more open with age. The closing of chromatin regions with age in
295 quiescent NSCs is consistent with findings of increased age-related repressive chromatin marks
296 such as H3K27me3 in other quiescent stem cells[67], including quiescent muscle satellite cells[68,69]
297 and hematopoietic stem cells[70]. The chromatin landscape of activated NSCs generally becomes

298 more permissive with age, consistent with the observation that reducing the repressive 5-
299 hydroxymethylcytosine (5hmC) mark in hippocampal NPCs mimics age-dependent defects[19].
300 Moreover, it is interesting to note that age-related chromatin changes are readily detectable in
301 activated NSCs, yet transcriptomic changes are very limited in these cells[25,26,28] and other cellular
302 systems[70-72]. Because the majority of dynamic chromatin changes that occur with age in NSCs
303 impact distal and intronic regulatory sites, which likely contain non-coding regulatory elements
304 such as enhancers, age-related chromatin changes in aNSCs may underlie longer-lasting changes
305 and manifest themselves transcriptionally more in downstream progenitors.
306
307 Cell adhesion emerged as a hallmark of NSC aging in our study. The migratory
308 properties of neuroblasts has started to be examined with age[44-47] and in the context of
309 innervating distal tumors[73]. But the changes in migration and adhesion in quiescent and activated
310 NSCs, the upstream NSC populations that give rise to migratory neuroblasts, remain largely
311 unknown. Our study reveals a dichotomy between changes to the adhesive/migratory properties
312 of quiescent and activated NSCs with age. As mechanical cell deformations affect the nucleus
313 and chromatin itself[74,75], epigenomic profiling might be especially sensitive to identifying
314 changes in the regulation of adhesion and migration in stem cells and their progeny.
315
316 A key question is the role of intrinsic factors vs. extrinsic factors in cell migration with
317 age. Age-related changes to the biomechanical properties of regenerative niches, such as
318 stiffness, have been shown to extrinsically induce age-related phenotypes[76]. Our findings in
319 cultured aNSCs/NPCs highlight the importance of intrinsic changes to cellular adhesion
320 pathways that change with age. Notably, aNSCs/NPCs isolated from an old brain retain

321 migratory impairment and increased occurence of force-producing adhesions even when
322 removed from the extrinsic effects of the niche. Understanding the contribution of intrinsic and
323 extrinsic responses, and how they influence each other during aging, will be critical to identify
324 strategies to boost regeneration and repair during aging.
325
326 Inhibiting Rho-associated kinase (ROCK), a regulator of cytoskeletal dynamics[57], with
327 the small molecule Y-27632 improves motility in aged activated NSCs and downstream
328 progenitors. Inhibition of ROCK has a profound impact on migration in a variety of cells,
329 including myoblasts, glioma cells, and microglia with different effects[77-84]. However, ROCK
330 inhibition has previously not been tested in aNSCs/NPCs during aging, and its effects on young
331 aNSCs/NPCs remain unclear: one study of human embryonic stem cell (ESC)-derived NSCs
332 showed decreased migration speed upon ROCK inhibition[85], while another study of NSCs
333 derived from postnatal and young adult mice showing increased migration speed upon ROCK
334 inhibition[64]. Here we show that ROCK inhibition eliminates focal adhesions and increases
335 migration in old aNSCs/NPCs. While ROCK has pleiotropic roles in aspects other than migration
336 (e.g. autophagy, apoptosis, vesicle dynamics, etc.), this protein kinase is a promising potential
337 target in the aging brain to restore aspects of migration notably in cases of injury and
338 neurodegenerative disease[86]. ROCK inhibitors are well tolerated in humans and have begun to be
339 studied in the context neurodegenerative disease[86] and could potentially be used to ameliorate
340 other age-dependent defects. Our study could help identify ways to restore proper migration of
341 NSCs and progenitors in the aging brain and in the context of brain injury.
342
343

Acknowledgements

We thank D. Wagh from the Stanford Functional Genomics Facility for Illumina NextSeq sequencing; the Stanford Shared FACS Facility for FACS use and support; K. Tsui and M. Bassik for assistance and use of the Incucyte Live Cell Imaging system; M. Buckley, G. A. Reeves, X. Zhao, P. P. Singh, and C.-K. Hu for their feedback and reading of the manuscript; M. Buckley, G. A. Reeves, P. P. Singh, and A. McKay for independently checking scripts used in this study; J. Butterfield for help with mouse husbandry and genotyping; and M. Bassik, J. Sage, and T. Wyss-Coray for guidance. This work was supported by P01AG036695 (A.B.), the Stanford Genome Training Program (R.W.Y.), a Stanford Graduate Fellowship (R.W.Y.), and a Genentech Foundation Pre-doctoral Fellowship (R.W.Y.).

Authors contributions

R.W.Y. and A.B. planned the study. R.W.Y. performed and analyzed all experiments, except for those indicated below. O.Y.Z. generated sections, performed immunostaining, and quantification for all *in vivo* experiments and participated in the planning of the study. B.Z. performed the RGD tension sensor experiments and analyzed the FRET data supervised by A.D.. M.S. generated the NSC deep learning model and performed motif enrichment supervised by A.K.. T.R. assisted in the *in vivo* NSC migration study. A.K. and A.D. also provided intellectual contribution. R.W.Y. and A.B. wrote the manuscript, with help from O.Y.Z., and all authors provided comments.

Competing Interests

The authors declare no competing interests.

Data availability

All raw sequencing reads and processed bam files for ATAC-seq libraries can be found under BioProject PRJNA715736.

Code availability

The code used to analyze genomic data in the current study are available in the Github repository for this paper (https://github.com/brunetlab/Yeo_RW_NSC_ATACseq).

390 **Methods**

391

392 **Laboratory animals**

393 For *in vivo* ATAC-seq libraries and immunofluorescence experiments with coronal sections, an
394 equal number of male and female GFAP-GFP (FVB/N background) mice[87] were pooled and
395 used. For ATAC-seq libraries generated from cultured NSCs, the SVZs from one male and one
396 female C57BL/6 mouse obtained from the NIA Aged Rodent colony were pooled and used. For
397 all other experiments, male C57BL/6 mice obtained from the NIA Aged Rodent colony were
398 used. In all cases, mice were habituated for more than one week at Stanford before use. At
399 Stanford, all mice were housed in either the Comparative Medicine Pavilion or the Neuro
400 Vivarium, and their care was monitored by the Veterinary Service Center at Stanford University
401 under IACUC protocols 8661.

402

403 **ATAC-seq library generation from freshly isolated cells**

404 We used fluorescence-activated cell sorting (FACS) to freshly isolate populations of endothelial
405 cells, astrocytes, quiescent NSCs (qNSCs), activated NSCs (aNSCs), and neural progenitor cells
406 (NPCs) from GFAP-GFP (FVB/N background) animals[87], as previously described[28]. Briefly, we
407 micro-dissected and processed the subventricular zones from young (3-5 months old) and old
408 (20-24 months old) GFAP-GFP mice following the previously described protocol[27] with the
409 addition of negative gating for CD45 (hematopoietic lineage) and sorting of endothelial cells
410 (CD31+) as previously described[28] (see Extended Data Fig. 1a). All FACS sorting was
411 performed at the Stanford FACS facility on a BD Aria II sorter, using a 100-μm nozzle at 13.1
412 pounds/square inch (psi), and Flowjo (v8) software was used for data analysis. Due to the rarity

413 of NSC lineage cells, we pooled sorted cells from 2 young male and 2 young female GFAP-GFP
414 mice for the young conditions (3-5 months old), and from 3 old male and 3 old female GFAP-
415 GFP mice for the old conditions (20-24 months old). For each respective library, we sorted either
416 2000 astrocytes, 2000 qNSCs (with the exception of a single library which only had 1670 cells),
417 800-1000 aNSCs, 2000 NPCs, or 2000 endothelial cells from GFAP-GFP animals for ATAC-seq
418 (see Supplementary Table 2). Young and old cells of the five cell types were sorted into 150 μL
419 of NeuroBasal-A medium (Gibco, 10888-022) with penicillin-streptomycin-glutamine (Gibco,
420 10378-016) and 2% B27 minus vitamin A (Gibco, 12587-010) in a 96-well V-bottomed plate
421 (Costar, 3894) and spun down at 300g for 5 min at 4°C. Sorted cells were washed with 100 μL
422 ice-cold 1x PBS (Corning, 21-040-CV), male and female cells were pooled by age and cell type,
423 and then spun down at 300g for 5 min at 4°C. Next, 50 μL of lysis buffer (10 mM Tris HCl pH
424 7.4 (Sigma, T2194), 10 mM NaCl, 3 mM $MgCl_2$ (Ambion, AM9530G), 0.10% NP-40 (Thermo,
425 85124)) was added to each well (alternating between young and old wells) and was immediately
426 spun down at 500g for 10 min at 4°C. Lysis buffer was carefully aspirated and 5 μL of
427 transposition mix (2.5 μL 2x Tagment DNA (TD) buffer, 2.25 μL nuclease-free H_2O, 0.25 μL
428 Tn5 transposase (Illumina, FC-121-1030)) was added to each well and pipetted 6x to resuspend
429 nuclei. Cells were incubated for 30 min at 37°C in a sealed 96-well plate and then briefly spun
430 down at 500g for 1 min to account for evaporation. Transposed DNA was then purified using the
431 Zymo DNA Clean & Concentrator kit (Zymo, D4014) and eluted in 20 μL of nuclease-free H_2O.
432 PCR amplification and subsequent qPCR monitoring was performed as previously described in
433 the original ATAC-seq protocol[29]. ATAC-seq libraries from young and old cells were amplified
434 with 11-14 PCR cycles and then purified using the Zymo DNA Clean & Concentrator kit (Zymo,
435 D4014) and eluted in 15 μL of nuclease-free H_2O. See below "*Library sequencing and ATAC-*

436 *seq quality control of in vivo and cultured NSCs*" for details on sequencing of ATAC-seq
437 libraries.
438
439 **Primary NSC cell culture**
440 To obtain primary cultures of adult NSCs for ATAC-seq, we micro-dissected and pooled SVZs
441 from pairs of male and female C57BL/6 mouse at a young age (3 months old) or an old age (23
442 months old) obtained from the NIA. To obtain primary cultures of adult NSCs for
443 immunofluorescence staining, migration assays, and force sensor assays, we micro-dissected the
444 SVZs from a single young C57BL/6 male (3-5 months old) or a single old C57BL/6 male (20-24
445 months old) obtained from the NIA (see Supplementary Table 1). In both cases, micro-dissected
446 SVZs were finely minced, suspended in 5 mL of PBS +0.1% Gentamicin (Thermo Fisher,
447 15710064) and spun down at 300g for 5 min at room temperature. We then dissociated SVZs by
448 enzymatic digestion using 5 mL of HBSS (Corning, 21-021-CVR) with 1% penicillin-
449 streptomycin-glutamine (Gibco, 10378-016), 1 U/mL Dispase II (STEMCELL Technologies,
450 07913), 2.5 U/mL Papain (Worthington Biochemical, LS003126), and 250 U/mL DNAse I
451 (D4527, Sigma-Aldrich), vortexed briefly, and left at 37°C for 40 min on a rotator. Following
452 digestion, the samples were spun down at 300g for 5 min at room temperature and resuspended
453 in 5 mL of NeuroBasal-A medium (Gibco, 10888-022) with 1% penicillin-streptomycin-
454 glutamine (Gibco, 10378-016) and 2% B27 minus vitamin A (Gibco, 12587-010) and triturated
455 repeatedly (20x) with 2-3 washes. Single-cell suspensions were then resuspended in "complete
456 activated media": Neurobasal-A (Gibco, 10888-022) supplemented with 2% B27 minus vitamin
457 A (Gibco, 12587-010), 1% penicillin–streptomycin–glutamine (Gibco, 10378-016), 20 ng/mL of
458 EGF (Peprotech, AF-100-15), and 20 ng/mL of bFGF (Peprotech, 100-18B). For passaging, cells

459 were dissociated with 1 mL Accutase (STEMCELL Technologies, 07920) for 5 min at 37°C,
460 washed once with 5 mL 1x PBS, and resuspended in "complete activated media" for expansion.
461 For quiescent conditions, quiescence was induced over 5-10 days by replacing "complete
462 activated media" with "complete quiescent media": Neurobasal-A (Gibco, 10888-022)
463 supplemented with 2% B27 minus vitamin A (Gibco, 12587-010), 1% penicillin–streptomycin–
464 glutamine (Gibco, 10378-016), 50 ng/mL of BMP4 (Biolegend 94073), and 20 ng/mL of bFGF
465 (Peprotech, 100-18B). For adherent cultures, we coated plates with PBS+Poly-D-Lysine (Sigma-
466 Aldrich, P6407, 1:20) for 30-120 min at 37°C, and washed plates 4x with 1x PBS prior to
467 seeding cells. All cell counting was performed using the Countess II FL Automated Cell Counter
468 (Life Technologies, AMQAF1000).
469
470 **ATAC-seq library generation from cultured NSCs**
471 To establish individual primary NSC cultures for ATAC-seq, we dissected and pooled the SVZs
472 from one male and one female C57BL/6 NIA mouse from either a young cohort (3 months old)
473 or an old cohort (23 months old). We dissociated and cultured NSCs as described above (in the
474 section "*Primary NSC cell culture*") to generate 4 young and 4 old biological replicates. At
475 passage 5, NSCs were plated at a density of 1.2 million cells per 6cm PDL-coated plate in
476 complete quiescent media for 8 days prior to sorting. At passage 7, NSCs from the same culture
477 were plated at a density of 1.5 million cells per 6cm plate onto PDL-coated plates in complete
478 activation media for 24 hours prior to sorting to synchronize quiescent and activated sorting
479 experiments. Plates were washed 3x with 1x PBS. Adherent qNSCs were lifted from the plate
480 using 1 mL of Accutase (STEMCELL Technologies, 07920) for 15 min at 37°C and adherent
481 aNSCs/NPCs were lifted from the plate using 1 mL of Accutase (STEMCELL Technologies,

482 07920) for 5 min at 37°C. The Accutase (STEMCELL Technologies, 07920) cell suspension was
483 diluted with 10 mL of 1x PBS, cells were spun down at 300g for 5 min, then resuspended in 200
484 μL of Neurobasal-A (Gibco, 10888-022) supplemented with 2% B27 minus vitamin A (Gibco,
485 12587-010), 1% penicillin–streptomycin–glutamine (Gibco, 10378-016) with propidium iodide
486 (BioLegend, 421301, 1:5000) for live/dead staining. Cells were kept on ice during all subsequent
487 steps.
488 Due to concern about differing levels of dead cells in the young vs. old cultures as well as the
489 contaminating influence of dead cells on ATAC-seq libraries, all samples were sorted using
490 fluorescence-activated cell sorting (FACS) based on the live gate (propidium iodide).
491 Specifically, 10,000-15,000 live cultured qNSCs and aNSCs/NPCs (see Supplementary Table 2)
492 were respectively sorted into 100 μL of NeuroBasal-A medium (Gibco, 10888-022) with
493 penicillin-streptomycin-glutamine (Gibco, 10378-016) and 2% B27 minus vitamin A (Gibco,
494 12587-010) in a 96-well V-bottomed plate (Costar, 3894) and spun down at 300g for 5 min at
495 4°C. Sorted cells were washed with 100 μL ice-cold 1x PBS (Corning, 21-040-CV), and spun
496 down at 300g for 5 min at 4°C. 50 μL of lysis buffer (10mM Tris HCl pH 7.4 (Sigma, T2194),
497 10mM NaCl, 3mM $MgCl_2$ (Ambion, AM9530G), 0.10% NP-40 (Thermo, 85124)) was added to
498 each well (alternating between young and old wells) which were immediately spun down at 500g
499 for 10 min at 4°C. Lysis buffer was carefully aspirated and 50 μL of transposition mix (12.5 μL
500 4x Tagment DNA (TD) buffer (gift from the Chang Lab), 35 μL nuclease-free H_2O, 2.5 μL Tn5
501 (gift from the Chang Lab)) was added to each well and pipetted 6x to resuspend nuclei. Cells
502 were incubated for 30 min at 37°C in a sealed 96-well plate and then briefly spun down at 500g
503 for 1 min to account for evaporation. Transposed DNA was then purified using the Zymo DNA
504 Clean & Concentrator kit (Zymo, D4014) and eluted in 20 μL of nuclease-free H_2O. PCR

505 amplification and subsequent qPCR monitoring was performed as previously described in the
506 original ATAC-seq protocol[29]. All libraries were amplified for 5 PCR cycles, and then an
507 additional 4 PCR cycles (based off of qPCR amplification curves), and then purified using the
508 Zymo DNA Clean & Concentrator kit (Zymo, D4014) and eluted in 15 μL of nuclease-free H_2O.
509

510 **Library sequencing and ATAC-seq quality control of *in vivo* and cultured NSCs**

511 We quantified individual library concentrations using a Bioanalyzer (High Sensitivity) and
512 pooled at a concentration of 5 nM for sequencing. Multiplexed libraries were sequenced using
513 NextSeq (400M) by the Stanford Functional Genomics Facility. To assess individual library
514 quality, individual library paired-end FASTQ files were processed using the Kundaje Lab's
515 ATAC-seq Pipeline (https://github.com/kundajelab/atac_dnase_pipelines) with default
516 parameters (using "-species mm10" and including "-auto_detect_adapter").
517 For *in vivo* ATAC-seq libraries generated from freshly isolated SVZ cells, libraries were
518 excluded based on insufficient read coverage (<10 million unique reads) or low peak calling
519 (<=20,000 peaks). In general, endothelial cell libraries were of worse quality than the other four
520 sorted cell types and we additionally censored one endothelial library with low bowtie alignment
521 (~92%) since all other libraries had a bowtie alignment of >= 95%.The high-quality libraries
522 were sequenced to a mean read depth of 29,187,427 unique reads (ranging from ~10-69 million
523 reads per library) (see Supplementary Table 2).
524 In general, ATAC-seq library quality was much better for cultured NSCs than freshly isolated
525 NSCs so we used a different set of metrics for quality control. For cultured NSCs, 1 library (out
526 of 4) from each condition was excluded to due to poor quality, defined as the library with the
527 lowest transcription start site (TSS) enrichment (<20 in all cases). Additionally, both young and

528 old quiescent cultures had one library that appeared highly anomalous (~2-fold greater fraction
529 of reads in peaks (FRiP) and TSS enrichment compared to every other library) so they were
530 additionally excluded to not confound results. The remaining 2-3 high-quality libraries per
531 condition were sequenced to a mean read depth of 26,271,688 unique reads (ranging from ~18-
532 42 million reads per library) (see Supplementary Table 2).
533

534 **ATAC-seq pipeline and processing**

535 Libraries that passed quality control were re-processed using the Kundaje Lab's ATAC-seq
536 Pipeline starting from de-duplicated BAM files to call peaks per multi-replicate condition. De-
537 duplicated, Tn5-shifted tagAlign files for each replicate were converted to BAM files (using
538 bedToBam (v2.29.2)) and sorted (using samtools sort (v1.10)) for downstream analysis. Peaks
539 per multi-replicate condition were selected using "overlap > optimal set" resulting in
540 approximately 20,000-90,000 peaks per *in vivo* condition (with a mean peakset size of 65,243
541 peaks) and approximately 90,000-150,000 peaks per cultured NSC condition (with a mean
542 peakset size of 118,987 peaks). To generate pooled read libraries, the 2-3 high-quality filtered,
543 de-duplicated BAM files for each condition were merged (using samtools merge (v1.10)), sorted
544 (using samtools sort (v1.10)), tn5-shifted (using deepTools alignmentSieve (v3.4.3)), and
545 indexed (using samtools index (v1.10)). All analysis was performed using the *mm10* mouse
546 genome ("TxDb.Mmusculus.UCSC.mm10.knownGene").
547

548 **Transcription start site (TSS) enrichment**

549 Transcription start site (TSS) enrichment heatmaps were generated with ngsplot.R (version
550 2.6.1)[88] using pooled, Tn5-shifted, sorted BAM files as inputs for each of the 10 conditions. All

551 analysis was performed using the *mm10* mouse genome

552 ("TxDb.Mmusculus.UCSC.mm10.knownGene").

553

554 **Generating consensus peaksets and count matrices**

555 To generate consensus peaksets for downstream analysis, BAM files and multi-replicate peak

556 files were loaded into a Large DBA object using Diffbind (v2.10.0)[89,90] "dba.count" with

557 parameters "minOverlap=0" and "score=DBA_SCORE_READS". We annotated peaks in the

558 consensus count matrices using the "annotatePeak" function of the package ChIPSeeker

559 (v1.18.0)[91] with parameters "tssREgion=c(-3000,3000)".

560

561 **Functional enrichment of genetic elements within global peaksets**

562 The "annotatePeak" function of ChIPSeeker (v1.18.0)[91] was used to identify the genetic element

563 identity of each chromatin peak within the multi-replicate peakset for each condition with

564 parameters (tssRegion=c(-3000, 3000), annoDb="org.Mm.eg.db"), and the annotation statistics

565 were extracted using "@annoStat". The different promoter terms "Promoter (<=1kb)",

566 "Promoter (1-2kb)", and "Promoter (2-3kb)" were manually grouped together under "Promoter",

567 and the two intron terms were manually grouped under "Intron".

568

569 **Principal Component Analysis (PCA)**

570 DESeq2 (v1.22.2)[92] was used to calculate dispersion estimates from raw consensus count

571 matrices and then variance stabilizing transformations were applied prior to visualization by

572 principal component analysis.

573 For *in vivo* ATAC-seq libraries generated from freshly isolated SVZ cells, PCA on all chromatin
574 peaks was generated using the global consensus peakset of 141,970 peaks. PCA consisting of all
575 young and old qNSC and aNSC libraries was generated using the count matrix consisting of
576 these 87,796 peaks. Based on peak annotations, the NSC consensus peakset was sub-divided into
577 a distal peakset (31,660 peaks), an intronic peakset (28,571 peaks), a promoter peakset (20,633),
578 and a putative enhancer (distal+intronic) peakset (60,231 peaks). For ATAC-seq libraries
579 generated from cultured NSCs, PCA was generated from the consensus peakset with 121,497
580 peaks. To compare how cultured NSCs compared to NSCs freshly isolated from the SVZ, we
581 performed PCA on the count matrix consisting of the 11 freshly isolated NSC libraries and the
582 10 cultured NSC libraries (156,963 peaks).
583
584 **Clustering freshly isolated ATAC-seq libraries for heatmap visualization**
585 To cluster and visualize all ATAC-seq libraries from freshly isolated SVZ cell populations
586 together, we generated a heatmap from the global consensus peakset (141,970 peaks) with
587 "cor()" using the default Pearson's correlation with the R library "pheatmap" (v1.0.12).
588
589 **Correlating ATAC-seq promoter accessibility and RNA-seq expression**
590 For young and old qNSCs and aNSCs freshly isolated from the SVZ, the average (VST-
591 normalized) chromatin accessibility value of each gene's promoter was associated with the
592 average (VST-normalized) RNA-seq[28] expression value for that gene. Promoters were binned in
593 deciles based on promoter accessibility and the association between promoter chromatin
594 accessibility and associated genic mRNA expression was plotted as deciled boxplots using R
595 (v3.5.2).

596

597 **Chromatin signal track visualization for freshly isolated NSCs**

598 Alignment tracks were visualized using IGV (v2.4.19). For each condition, the BAM file for a
599 single representative library (see Supplementary Table 2) was normalized by Reads per Kilobase
600 per Million mapped reads (RPKM-normalization) and converted to a bigwig file using deepTools
601 (v3.4.3) with the following parameters: "--extendReads 100 --normalizeUsing RPKM --binSize
602 10".

603

604 **Differential peak calling**

605 To identify differentially accessible peaks that change with age for each cell type, count matrices
606 consisting of young and old replicates within a single cell type were generated using Diffbind
607 (v2.10.0)[89,90] as described above (see *Generating consensus peaksets and count matrices*).
608 Differential peak calling was accomplished using EdgeR (v3.24.3)[93,94] with the following
609 parameters for "dba.analyze": bCorPlot=FALSE, bParallel=TRUE, bTagwise=FALSE,
610 bFullLibrarySize=TRUE, bReduceObjects=FALSE,method=DBA_EDGER". For all
611 comparisons, differential peaks were obtained using a false discovery rate (FDR) threshold of
612 0.05 (see Supplementary Table 3). Differential peaks were annotated and associated with their
613 closest gene using the "annotatePeak" function of the package ChIPSeeker (v1.18.0)[91] with
614 parameters "tssREgion=c(-3000,3000)". For the differential peaks that change with age in the
615 freshly isolated qNSC and aNSC libraries respectively, differential peaks were aligned to the
616 *mm10* chromosomes using the "covplot()" function in ChIPSeeker (v1.18.0)[91] for ease of
617 visualization. It should be noted that the opposing directionality of dynamic peak changes with

618 age was only observed in freshly isolated qNSCs and aNSCs (whereas cultured qNSCs and
619 aNSCs/NPCs both generally show an opening of chromatin peaks with age).
620
621 **Functional enrichment of genetic elements within differential NSC peaksets**
622 The differentially accessible peaks that change with age in the freshly isolated qNSC and aNSC
623 conditions respectively were separated into sets that close with age or open with age and were
624 annotated with the "annotatePeak" function of ChIPSeeker (v1.18.0)[91] with parameters
625 (tssRegion=c(-3000, 3000), annoDb="org.Mm.eg.db"). The annotation statistics from
626 "@annoStat" were manually grouped into 4 categories: "Distal Intergenic", "Intron",
627 "Promoter", and "Other".
628
629 **Nucleosome peak calling**
630 To identify whether the chromatin landscapes of young and old freshly isolated qNSCs and
631 aNSCs had different levels of heterochromatin-associated nucleosomes, we used the package
632 NucleoATAC (v0.2.1)[95]. We called nucleosome peaks from our ATAC-seq data using
633 "nucleoatac run" with parameters: "--bed" the multi-replicate peak files for each condition, "--
634 bam" pooled, down-sampled (to 30 million unique reads), Tn5-shifted BAM files, and "--fasta"
635 the mm10 Mus musculus UCSC genome. The number of nucleosome peaks for each condition
636 were taken from the "*.nucmap_combined.bed" files and plotted with R (v3.5.2).
637
638 **Gene Ontology (GO) Biological Pathway Enrichment of differentially accessible chromatin**
639 **peaks**

640 Differentially accessible peaks were associated with nearby genes using the ChIPSeeker
641 (v1.18.0)[91] function "annotatePeak". Gene lists were uploaded to the online tool EnrichR[96,97] and
642 top ranked GO terms from "GO Biological Process 2018" were extracted for pathways that
643 change with age (see Supplementary Table 4). Selected GO terms were ranked by *P*-value and
644 plotted for visualization in R (v3.5.2).
645
646 **Gene Ontology (GO) Biological Pathway Enrichment of genes driving PC axes**
647 In order to identify what biological processes were associated with peaks driving the principal
648 components (PCs) in the PCA of young and old freshly isolated qNSCs and aNSCs, the top 1000
649 peaks driving the principal components (either negatively or positively) were extracted and
650 associated with genes (see Supplementary Table 6). The genes (under header "Symbol")
651 associated with these peaks were uploaded to EnrichR to identify top ranked GO terms from
652 "GO Biological Process 2018" (see Supplementary Table 7). The top 6 GO terms for PC2
653 negative peaks (grouping old qNSCs and young aNSCs) and PC2 positive peaks (grouping
654 young qNSCs and old aNSCs) were ranked by *P*-value and plotted in R (v3.5.2) for
655 visualization.
656
657 **Chromatin peak heatmaps within cell adhesion pathways**
658 To visualize how aging affects chromatin peak accessibility associated with cell adhesion, genes
659 associated with differential peaks that change with age in either freshly isolated qNSCs or aNSCs
660 respectively were intersected with the "Cell Adhesion" GO gene list (GO:0007155)
661 (http://www.informatics.jax.org). Differential peak accessibility levels were plotted as heatmaps
662 using "pheatmap" (v1.0.12) in R (v3.5.2) (TMM-normalized read counts, scaled row-wise).

663

664 **Homer Motifs**

665 To identify transcription factors that could be involved in aging, motif enrichment was
666 performed using the Homer tool "findMotifsGenome.pl" (v4.11.1)[98] with parameters "-size
667 given -mask" on differential peak lists (only Known Motifs are reported here) (see
668 Supplementary Tables 5). Since many enriched motifs were highly redundant, selected motifs
669 were grouped by identity and plotted for visualization (ranked by p-value) in R (v3.5.2).

670

671 ***De novo* transcription factor binding patterns using a deep learning model and TF-**
672 **MoDISco**

673 Binary open/closed chromatin was learned using a deep learning model (Basset architecture, i.e.
674 3 convolution layers, 2 fully connected layers followed by logit)[99] for each of the young and old
675 freshly isolated cell types (except for endothelial cells which were omitted due to inferior library
676 quality). For model training, naïve overlap peaks were used as positive examples (i.e. open
677 chromatin) and sequences from the rest of the genome were used as negative examples (i.e.
678 closed chromatin). The size of each example is a 1kb sequence, each taken with 50bp strides of
679 size 200 initially and expanded to 1kb later on. Sequences with at least 50% overlap with the
680 naïve peaks are positive examples and the rest are the negative examples. Each model was tested
681 on chromosome 1 and trained on rest of the chromosomes. Their genome-wide performance
682 ranged from 0.22 to 0.5 auPRC (Area Under precision recall curve) depending on the imbalance
683 ratio of positive and negative examples for the sequence. Notably, amongst all of the different
684 conditions, model performance for young and old qNSCs and aNSCs were among the best
685 compared to other cell types (above 0.45). We trained and tested our model performances for 10-

686 folds; since performance hardly varied across folds, we conducted rest of our analysis on the 1st
687 fold of models. Details of the performances across each sample and each folds, the correlation of
688 the model performances with the imbalance ratio can be found here -
689 http://mitra.stanford.edu/kundaje/msharmin/report/nsc_reports/NSC.html
690 To identify importance score on the sequences, for each sample we treated the peaks as 1kb
691 sequence centered around the peak summit and interpreted each base using DeepLIFT[35].
692 DeepLIFT assigns a score for each base of the sequence learned from the model based on how
693 important that base would be with respect to a set of background sequences. Next, we take the
694 importance score tracks and learned the over-represented important sequence patterns using
695 MoDISco[36,37]. MoDISco takes the importance scores, identifies the high scoring sub-sequences
696 (called seqlets) and cluster the seqlets into over-represented patterns called MoDISco-patterns.
697 Notably, given that deep learning models do not give 100% accuracy, we tried to pick the true-
698 positive peaks for finding MoDISco patterns. To clarify further, we interpreted only the peaks,
699 i.e. knowing that peaks are positive examples for the model. Hence, to pass the importance
700 scores to MoDISco, we filtered the peaks with high-scores as positive by the deep learning
701 model. The high-score is defined by the calibrated model-score
702 ([https://github.com/kundajelab/abstention]) which gives 50% FDR cut off for the model
703 performance. Each MoDISco pattern for each sample is then matched with CISBP 2.00 motif
704 database and the matched motifs are listed into separate html files per sample (and per set of
705 differential regions) linked from here
706 (http://mitra.stanford.edu/kundaje/msharmin/report/nsc_reports/NSC.html).
707 For finding MoDISco pattern in the differential regions we took the previously selected regions
708 (as obtained using DiffBind[89,90]) and retained the regions with 50% overlap with one of the

709 defined 1kb peaks as described above. Then we filtered the differential peak sets based on true-
710 positive peak sets called by the model and used their importance scores on TF-MoDISco to find
711 the set of differential MoDISco patterns.
712
713 **Single cell RNA-seq expression values for Cell Adhesion genes**
714 Single cell gene expression data of the SVZ[25] consisting of 14,685 cells (8,884 cells from young
715 and 5,801 cells from old) were used in order to identify how gene expression differs by cell type
716 and age at single-cell resolution using an orthogonal dataset.
717 Single cell gene expression values for qNSCs/astrocytes, aNSCs/NPCs, and neuroblasts were
718 extracted and subset based on genes from the "Cell Adhesion" GO gene list (GO:0007155). For
719 each single cell within a cell population, the expression levels of cell adhesion genes were
720 summed. The cumulative expression level of adhesion genes comparing young
721 qNSCs/astrocytes, aNSCs/NPCs, and neuroblasts was visualized using violin plots with R
722 (v3.5.2). The cumulative expression level of adhesion genes comparing young and old
723 qNSCs/astrocytes, and young and old aNSCs/NPCs was visualized using violin plots with R
724 (v3.5.2). Statistical comparisons between conditions was performed in R using a two-tailed
725 Mann-Whitney test.
726 Using the same dataset, we investigated the relationship between cell cycle phase and cellular
727 adhesion. To this end, t-SNE analysis was performed on SVZ cells as previously described[25]
728 using the Seurat package (v3.1.5)[100]. The 8,884 single cells from the young SVZ were colored
729 based on expression of genes from the "Cell Adhesion" GO gene list (GO:0007155) as well as
730 by their cell cycle phase for side-by-side comparison.
731

732 We plotted the relationship between Seurat's "S phase score" and the cumulative expression of
733 genes from the "Cell Adhesion" GO gene list (GO:0007155) in qNSCs/astrocytes, aNSCs/NPCs,
734 and neuroblasts, and found no evidence of a correlative relationship between cellular adhesion
735 and proliferative propensity. For this analysis, each cell population was downsampled to the
736 number of old cells (480 qNSCs/astrocytes, 82 aNSCs/NPCs, and 146 neuroblasts).
737

738 **Ingenuity Pathway Analysis (IPA)**

739 Genes associated with differentially accessible peaks (FDR<0.05) that open in old aNSCs freshly
740 isolated from the SVZ were uploaded to Ingenuity Pathway Analysis (IPA) (v1.16)[101] (QIAGEN
741 Inc., https://www.qiagenbioinformatics.com/products/ingenuitypathway-analysis) to identify
742 age-related regulatory changes (see Supplementary Table 8). For each peak-associated gene, we
743 uploaded the log fold-change, p-value, and FDR (q-value) and based the IPA analysis on FDR.
744 Statistical enrichment of pathways was reported with *P*-values calculated by IPA using Fisher's
745 Exact Test.
746

747 **Migration assay of cultured qNSCs and aNSCs/NPCs using live cell imaging**

748 aNSCs/NPCs were cultured in complete activated media until Passage 2-4 and then seeded at a
749 density of 200,000 cells per well in a PDL-coated 12-well plate with complete activated media
750 treated with vehicle (H_2O) or 10μM Y-27632 (dissolved in H_2O) (Tocris, 1254). After 48 hours,
751 adherent aNSCs/NPCs were passaged with 500 μL of Accutase (STEMCELL Technologies,
752 07920), and resuspended in in Neurobasal-A (Gibco, 10888-022) supplemented with 2% B27
753 minus vitamin A (Gibco, 12587-010) and 1% penicillin–streptomycin–glutamine (Gibco, 10378-
754 016) with propidium iodide (BioLegend, 421301, 1:5000) for live/dead staining. 1000 live (PI-)

755 cells per well were sorted with flow cytometry using the BD PICI onto PDL-coated Incucyte
756 ImageLock 96-well plates (Essen BioScience, 4379) containing 100 μL of complete activated
757 media with 10 nM Syto64 (Invitrogen, S11346, Lot #8344573) and either vehicle (H_2O) or
758 10μM Y-27632 (dissolved in H_2O) (Tocris, 1254). The ImageLock plate was immediately
759 brought to the Incucyte Zoom or Incucyte S3 live imaging system to image (with Phase and RFP
760 channels) at 37°C every 30 min for 20 hours with the 20X objective. After 20 hours, the cell
761 media was washed 2x with PBS and then replaced with 100 μL of complete quiescent media.
762 Media was changed every other day for 7 days to induce quiescence. The media was then
763 replaced with complete quiescent media supplemented with 10 nM Syto64 (Invitrogen, S11346,
764 Lot #8344573) prior to imaging. Wells were imaged (with Phase and RFP channels) using either
765 the Incucyte S3 or Incucyte Zoom system with the 20X objective every hour for 20 hours at
766 37°C. Three images (from different parts of the well) at each timepoint were taken for each well
767 and tracked cell metrics were summed across these three images. Cell migration tracking was
768 performed using Imaris (v9.3.0). Every image stack was manually curated to ensure that cell
769 tracking was correctly performed (e.g. that automated cell tracking was not incorrectly labelling
770 debris and that cell tracks accurately follow individual cells). "Track Velocity" was output for
771 visualization with Prism (v8) and *P*-values were calculated with a two-tailed Mann-Whitney test
772 comparing both single cell values as well as sample mean values (where single cell velocities are
773 averaged by animal).
774
775 **Matrigel migration assay**
776 Activated NSCs/NPCs were cultured in complete activated media until Passage 4-6, passaged
777 with Accutase (STEMCELL Technologies, 07920), and resuspended in complete activated

778 media at a concentration of 100,000 cells/μL. Matrigel (Corning, 354230, Lot #8344573) was
779 diluted 1:2 in cold F12:DMEM (Gibco, 11-330-057) while on ice to prevent solidification, and
780 50 μL was immediately added per well to a 96-well plate. The 96-well plate was moved to the
781 37°C incubator for 3 hours prior to spotting 50,000 cells (in a volume of 0.5 μL) directly to the
782 center of the Matrigel-coated well. The plate was returned to the 37°C incubator for 15-30 min to
783 allow for cells to adhere. 150 μL of complete activated media (treated with vehicle (H_2O) or
784 10μM Y-27632 (dissolved in H_2O) (Tocris, 1254)) was very carefully added to each well, and
785 the 96-well plate was placed in either the Incucyte Zoom or Incucyte S3 live imaging system to
786 image every 6 hours for 48 hours using the 4x objective to image the entire well. For each
787 biological replicate, 1-4 technical replicates were quantified to account for difficulties in spotting
788 0.5 μL volumes, and the distances migrated at each timepoint were averaged among technical
789 replicates. We manually quantified invasion distance, defined as the maximum distance from the
790 initial spotting perimeter to the outermost cell body, using Fiji (v2)[102]. Neither imaging nor
791 analysis was performed in a blinded manner. *P*-values were calculated with a two-tailed Mann-
792 Whitney test at each 12-hour timepoint.
793
794 **Immunofluorescence staining of SVZ coronal sections**
795 Four young (4 months old) and four old (18-26 months old) GFAP-GFP animals of both sexes (2
796 male and 2 female animals per age condition) were subjected to intracardiac perfusion with 4%
797 paraformaldehyde (Electron Microscopy Sciences, 15714) in PBS. Brains were post-fixed
798 overnight in 4% paraformaldehyde (Electron Microscopy Sciences, 15714) and then dehydrated
799 in 30% sucrose (Sigma-Aldrich, S3929) for 72 hours. Brains were embedded in Tissue-Tek
800 optimal cutting temperature (O.C.T.) compound (Electron Microscopy Sciences, 62550),

801 sectioned in 16 μm coronal slices using a cryostat (Leica CM3050S), and then mounted on glass
802 slides (Fisher Scientific, 12-550-15). To ensure a similar anatomic region of the lateral ventricle
803 was being analyzed in each animal, the corpus callosum was first identified in the sections. This
804 section was selected to be stained for cell markers. Two additional sections, approximately 100
805 μm and 200 μm anterior to the corpus callosum were also selected to be stained for cell markers
806 for a total of 3 sections per animal. To perform immunofluorescent staining, sections were
807 washed with PBS and then permeabilized with ice-cold methanol + 0.1% Triton X-100 (Fisher
808 Scientific, BP151) for 15 min. Slides were washed 3x with PBS for 5 min. Antigen retrieval was
809 performed in 10mM sodium citrate buffer (pH 6.0) (2.94 g Tri-sodium citrate dihydrate (Sigma-
810 Aldrich, S1804) in 1000 mL milliQ H_2O adjusted to pH 6.0 with 1N HCl) + 0.05% TWEEN 20
811 (Sigma-Aldrich, P1379-1L) at 85°C for 2 hours. Slides were then cooled to room temperature for
812 20 min, and sections were blocked with 5% Normal Donkey Serum (NDS) (ImmunoReagents
813 Inc., SP-072-VX10) and 1% BSA (Sigma, A7979) in PBS for 30 min at room temperature.
814 Primary antibody staining was performed overnight at 4°C in 5% Normal Donkey Serum and 1%
815 BSA in PBS. Primary antibodies used were the following: Ki67 (Invitrogen, SolA15 [1:200])
816 and GFAP (Abcam, ab53554, [1:500]). Sections were then washed 3x with PBS and 0.2%
817 TWEEN 20 for 10 min at room temperature followed by two PBS washes for 15 min. Secondary
818 antibody staining was performed at room temperature for 2 hours in 5% NDS and 1% BSA in
819 PBS. Secondary antibodies used were the following: Donkey anti-Goat 488 (Sigma Aldrich,
820 SAB460032-250UL [1:1000]), and Donkey anti-Rat 594 (Life Technologies, A21209 [1:1000]).
821 DAPI (ThermoFisher, 62248 [1:500]) was added during secondary antibody staining. Sections
822 were washed 3x for with PBS and 0.2% TWEEN 20 for 10 min at room temperature followed by
823 3 PBS washes for 5 min. Sections were mounted with ProLong Gold Antifade Mountant with

824 DAPI (ThermoFisher, P36931) and visualized with a Nikon Eclipse Ti confocal microscope
825 equipped with a Zyla sCMOS camera (Andor) and NIS- Elements software (AR 4.30.02, 64-bit).
826 Multiple Z-stacks using the 60x objective were captured to image the entire length of the SVZ
827 from one hemisphere per section. These Z-stacks (30 slices per stack) were transformed into a Z-
828 projection (max intensity) and quantified using a custom pipeline. GFAP-positive and Ki67-
829 positive nuclei were identified as aNSCs. GFAP-positive and Ki67-negative nuclei were
830 identified as qNSCs/astrocytes. Although rare, NSCs lining blood vessels were censored in the
831 analysis. The center of each NSC nuclei was chosen as a reliable and consistent fixed point to
832 assess cell localization. Distances from the ventricle were calculated by measuring Euclidean
833 distance from the center of the nucleus of each cell of interest to the ventricle border in Fiji (v2).
834 Neither imaging nor analysis was performed in a blinded manner. *P*-values were calculated with
835 a two-tailed Mann-Whitney test. For immunofluorescent images in this manuscript, brightness
836 and contrast were adjusted in Fiji (v2) to enhance visualization. These adjustments were
837 performed after all data quantification was complete. The same settings were applied to all
838 images shown for each experiment.
839
840 ***In vivo* SVZ migration by EdU-labelling**
841 Young (2-3 months) and old (21 months) male C57BL/6 animals were intraperitoneally injected
842 with 5-ethynyl-2'-deoxyuridine (EdU) (Fisher Scientific, A10044) (resuspended in PBS at 5
843 mg/mL) at a dose of 50 mg/kg either 4 hours, 2 days, or 7 days prior to intracardiac perfusion
844 with 4% paraformaldehyde (PFA) (Electron Microscopy Sciences, 15714) in PBS. Brains were
845 post-fixed overnight in 4% PFA and then dehydrated in 30% sucrose (Sigma-Aldrich, S3929) for
846 72 hours. Brains were embedded in Tissue-Tek optimal cutting temperature (O.C.T.) compound

847 (Electron Microscopy Sciences, 62550) and sectioned in 16 μm sagittal slices using a cryostat
848 (Leica CM3050S) that were then mounted on glass slides (Fisher Scientific, 12-550-15).
849 Immunofluorescent staining of sagittal sections was performed as above (see
850 *Immunofluorescence staining of SVZ coronal sections*) except that the CliCK-IT EdU Alexa
851 Fluor 488 imaging protocol (Thermo Fisher Scientific, C10337) was performed for 30 min at
852 room temperature prior to blocking. The following primary antibodies were used: Ki67
853 (Invitrogen, SolA15 [1:200]) and DCX (Cell Signaling Technologies, 4604 [1:500]). The
854 following secondary antibodies were used: Donkey anti-Rabbit Alexa 568 (Invitrogen, A10042
855 [1:500]) and Goat anti-Rat Alexa 647 (Invitrogen, A21247 [1:500]). DAPI (1 mg/mL)
856 (ThermoFisher, 62248) was included at a concentration of 1:500 with the secondary antibody
857 mix. Sections were mounted with ProLong Gold Antifade Mountant with DAPI (ThermoFisher,
858 P36931) and visualized with a Zeiss LSM 900 confocal microscope equipped with Zeiss ZEN
859 Blue 3.0 software.
860 Multiple sections per brain were stained and imaged to determine the optimal depth to capture
861 SVZ/RMS migration and the most appropriate section per animal was imaged and quantified.
862 Appropriate sections were selected based on presence of an intact RMS as judged by a stream of
863 DCX-positive cells connecting the SVZ to the OB. Images of sagittal sections were captured
864 using a 5x objective and 9x3 images (for a total of 27) were automatically stitched together using
865 the Zeiss ZEN Blue 3.0 software. For quantification, EdU-labelled nuclei were counted using Fiji
866 (v2)[102]. Briefly, every image was converted to 8-bit, the threshold was adjusted ((90,255) for
867 replicate 1 and (70,255) for replicate 2), watershed was applied to the image and EdU-labelled
868 nuclei were counted with "Analyze Particles (size (micron^2): (20-infinity) for replicate 1 and 2,
869 and circularity: (0.2-1.00) for replicate 1)". EdU-labelled nuclei were quantified in three regions

870 (SVZ, RMS, and OB) which were manually defined using a hand-drawn region of interest (ROI)
871 for each slide. To calculate distances of EdU+ cells from the ventricle, images of the SVZ from
872 the sagittal sections used above were captured using a 20x objective and subject to the same
873 analysis as described in (*Immunofluorescence staining of SVZ coronal sections).* EdU+ cells
874 were classified as aNSCs/NPCs if they were Ki67-positive and DCX-negative and as neuroblasts
875 if they were DCX-positive. One old 7-day post-injection replicate from the first experiment was
876 censored due to a failed intraperitoneal EdU injection and one young 7-day post-injection
877 replicate from the second experiment was censored due to lack of high quality sections at the
878 appropriate depth. Neither imaging nor analysis was performed in a blinded manner. *P*-values
879 were calculated with a two-tailed Mann-Whitney test.
880
881 **Immunofluorescence staining of young and old cultured NSCs**
882 NSCs were cultured as described above (see *Primary NSC culture*) in complete activated media
883 until Passage 2-3 and then seeded at a density of 200,000 cells per well in a PDL-coated 12-well
884 plate with complete activated media. After 48 hours, adherent aNSCs/NPCs were passaged with
885 500 μL of Accutase (STEMCELL Technologies, 07920), and resuspended in Neurobasal-A
886 (Gibco, 10888-022) supplemented with 2% B27 minus vitamin A (Gibco, 12587-010) and 1%
887 penicillin–streptomycin–glutamine (Gibco, 10378-016) with propidium iodide (BioLegend,
888 421301, 1:5000) for live/dead staining. 1000 live (PI-) cells per well were FACS sorted using the
889 BD PICI onto PDL-coated glass-bottomed 96-well plates (Cellvis, P96-1.5H-N) containing 100
890 μL of either complete activated media or complete quiescent media. After 24 hours for the
891 activated plates and 5-7 days for the quiescent plates, the sorted wells were washed 1x with PBS,
892 then fixed with 4% paraformaldehyde (Electron Microscopy Sciences, 15714) for 15 min. Wells

893 were washed 4x with PBS and then stored, wrapped in parafilm, at 4°C until
894 immunofluorescence staining. Cells were washed 2x with PBS and permeabilized with 0.1%
895 Triton X-100 (Fisher Scientific, BP151). Blocking was performed for 30 min with 1% BSA
896 (Sigma, A7979) in PBS. Primary staining was conducted for 1 hour at room temperature with
897 phalloidin (Invitrogen, A12379, 665217, 1:500) resuspended in 1% BSA (Sigma, A7979). Wells
898 were then washed 4x with PBS and secondary staining was performed for 1 hour at room
899 temperature with Donkey anti-Rabbit Alexa 568 (Invitrogen, A10042, 1:500) resuspended in 1%
900 BSA (Sigma, A7979). Wells were washed 4x with PBS+0.2% TWEEN 20 (Sigma-Aldrich,
901 P1379-1L), then 4x with PBS prior to imaging. Imaging was performed on a Nikon Eclipse Ti
902 confocal microscope equipped with a Zyla sCMOS camera (Andor) and NIS- Elements software
903 (AR 4.30.02, 64-bit) using the 60x objective. Quantification of immunofluorescence staining of
904 F-actin was done using a custom pipeline in Fiji (v2)[102]. Fluorescence intensity in regions of
905 high-density phalloidin staining were quantified as a proxy for bundled actin. Briefly, images
906 were converted to 8-bit, inverted and an intensity threshold was manually set in the phalloidin
907 channel to generate a mask. The same threshold values were used for all images across all
908 conditions in each individual experiment. The sum of pixel intensity within the cell mask
909 (RawIntDen) was then used to determine fluorescence intensity for each cell. For each
910 experiment, values were normalized by dividing each cell's fluorescence intensity by the mean
911 fluorescence intensity of all cells in the young condition. Neither imaging nor analysis was
912 performed in a blinded manner. *P*-values were calculated with a two-tailed Mann-Whitney test.
913

914 **RGD molecular tension sensor FRET measurements of cultured NSCs**

915 Sensors containing a minimal RGD sequence derived from fibronectin

916 (TVYAVTGRGDSPASSAA) were expressed, purified, and labeled with AlexaFluor-546 and -
917 647, and coverslips passivated with maleimide polyethylene glycol (PEG) succinimidyl
918 carboxymethyl ester (JenKem Technology, A5003-1) were prepared as previously
919 described[55,103]. Flow chambers for imaging were prepared as described[103] with slight
920 modifications. 8-well flow chambers (Grace BioLabs, #622505, ~55µL channel volume) were
921 attached to PEGylated coverslips as previously described[104]. Chambers were incubated with 300
922 nM double-labeled sensor at room temperature for 45 min. The chambers were then washed with
923 150 µL of PBS for 1 min to prevent non-specific cell attachment. 60 µL of cell suspensions at a
924 density of 300,000-400,000 cells/mL were added to the channels, and the chambers were
925 incubated for 3 hours at 37°C and 5% CO2 in complete activation media to allow cells to spread.
926 Chambers were then washed with 150 µL of warm media, and brightfield and FRET
927 measurements were made immediately after and acquired with an objective heater (Bioptechs)
928 set to 37°C. For measurements on cells treated with Y-27632, complete activation media was
929 supplemented with 10µM Y-27632 (dissolved in H_2O) (Tocris, 1254)) for cell suspensions and
930 media washes.
931 We limited our measurements and analysis to individual cells that looked well-spread in
932 brightfield and cell clusters of no more than 5 cells in which cell outlines could be clearly
933 distinguished. FRET fluorescence measurements were performed with objective-type total
934 internal reflection fluorescence (TIRF) microscopy on an inverted microscope (Nikon TiE) with
935 an Apo TIRF 100× oil objective lens, numerical aperture 1.49 (Nikon) as described previously[55]
936 and controlled using Micromanager[105]. Samples were excited with 532-nm (Crystalaser) or 635-
937 nm (Blue Sky Research) lasers. Emitted light passed through a quad-edge laser-flat dichroic with
938 center/bandwidths of 405/60 nm, 488/100 nm, 532/100 nm, and 635/100 nm from Semrock Inc.

939 (Di01-R405/488/532/635-25×36) and corresponding quad-pass filter with center/bandwidths of
940 446/37 nm, 510/20 nm, 581/70 nm, 703/88 nm band-pass filter (FF01-446/510/581/703-25).
941 Donor and acceptor images were taken through separate additional cubes stacked into the light
942 path (donor: 550 nm long-pass; acceptor: 679/41 nm and 700/75 nm) and recorded on a
943 Hamamatsu Orca Flash 4.0 camera.
944 Images were prepared in Fiji (v2)[102] and analyzed using custom MATLAB scripts, in which
945 FRET efficiencies were computed and thresholded to identify adhesions and quantify forces
946 within adhesions. An appreciable fraction of cultured aNSCs/NPCs seeded on RGD molecular
947 tension sensors did not exhibit distinct focal adhesion patterns upon analysis, potentially
948 reflecting cells generating tractions below the sensitivity threshold of the assay. To compare the
949 adhesive forces of these cells with those that had distinct focal adhesions, we used the average
950 FRET/force values underneath the entire cell body as a metric for the adhesive strength in cells
951 without adhesions. While we observed significant differences in fractions of old and young
952 aNSCs exhibiting force-generating adhesions through this analysis, we observed that these
953 differences may be driven by divergent phenotypes in integrin-mediated force upon contact with
954 other cells. For the cells that were imaged and analyzed, we observed little difference in focal
955 adhesion phenotype in isolated cells but sharp differences in phenotype in cells that were in
956 small clusters. These data are aggregated in Fig. 4e,f, Fig. 5d,e, and Extended Fig. 8.
957
958 **Immunofluorescence staining of cultured NSCs treated with ROCK inhibition**
959 aNSCs/NPCs were cultured as described above (see *Primary NSC culture*) in complete activated
960 media until Passage 2-3 and then seeded at a density of 200,000 cells per well in a PDL-coated
961 12-well plate with complete activated media treated with vehicle (H_2O) or 10μM Y-27632

962 (dissolved in H_2O) (Tocris, 1254). After 48 hours, adherent aNSCs/NPCs were passaged with
963 500 μL of Accutase (STEMCELL Technologies, 07920), and resuspended in Neurobasal-A
964 (Gibco, 10888-022) supplemented with 2% B27 minus vitamin A (Gibco, 12587-010) and 1%
965 penicillin–streptomycin–glutamine (Gibco, 10378-016) with propidium iodide (BioLegend,
966 421301, 1:5000) for live/dead staining. 1000 live (PI-) cells per well were FACS sorted using the
967 BD PICI onto PDL-coated glass-bottomed 96-well plates (Cellvis, P96-1.5H-N) containing 100
968 μL of complete activated media treated with vehicle (H_2O) or 10μM Y-27632 (dissolved in H_2O)
969 (Tocris, 1254). After 24 hours, the sorted wells were washed 1x with PBS, then fixed with 4%
970 paraformaldehyde (Electron Microscopy Sciences, 15714) for 15 min. Wells were washed 4x
971 with PBS and then stored, wrapped in parafilm, at 4°C until immunofluorescence staining.
972 Staining and quantification of old cultured aNSCs/NPCs for ROCK inhibition experiments was
973 otherwise performed in the same manner as described above (see *Immunofluorescence staining*
974 *of young and old cultured NSCs*).
975

976 **Statistical analyses**

977 For all experiments, young and old conditions were processed in an alternate manner rather than
978 in two large groups, to minimize the group effect. We did not perform power analyses, though
979 we did take into account previous experiments to determine the number of animals needed. To
980 calculate statistical significance for experiments, all tests were two-sided Mann-Whitney tests
981 (with the exception of Fisher's Exact Tests which are noted in Figure Legends). Results from
982 individual experiments and all statistical analyses are included in Supplementary Table 1.

983

984 **References**

985 1. Bond, A.M., Ming, G.L. & Song, H. Adult Mammalian Neural Stem Cells and
986 Neurogenesis: Five Decades Later. *Cell Stem Cell* **17**, 385-95 (2015).
987 2. Hattiangady, B., Rao, M.S. & Shetty, A.K. Plasticity of hippocampal stem/progenitor
988 cells to enhance neurogenesis in response to kainate-induced injury is lost by middle age.
989 *Aging Cell* **7**, 207-24 (2008).
990 3. Conover, J.C. & Shook, B.A. Aging of the subventricular zone neural stem cell niche.
991 *Aging Dis* **2**, 49-63 (2011).
992 4. Navarro Negredo, P., Yeo, R.W. & Brunet, A. Aging and Rejuvenation of Neural Stem
993 Cells and Their Niches. *Cell Stem Cell* **27**, 202-223 (2020).
994 5. Nicaise, A.M., Willis, C.M., Crocker, S.J. & Pluchino, S. Stem Cells of the Aging Brain.
995 *Front Aging Neurosci* **12**, 247 (2020).
996 6. Rao, M.S., Hattiangady, B. & Shetty, A.K. Status epilepticus during old age is not
997 associated with enhanced hippocampal neurogenesis. *Hippocampus* **18**, 931-44 (2008).
998 7. Mirzadeh, Z., Merkle, F.T., Soriano-Navarro, M., Garcia-Verdugo, J.M. & Alvarez-
999 Buylla, A. Neural stem cells confer unique pinwheel architecture to the ventricular
1000 surface in neurogenic regions of the adult brain. *Cell Stem Cell* **3**, 265-78 (2008).
1001 8. Shen, Q. *et al.* Adult SVZ stem cells lie in a vascular niche: a quantitative analysis of
1002 niche cell-cell interactions. *Cell Stem Cell* **3**, 289-300 (2008).
1003 9. Tavazoie, M. *et al.* A specialized vascular niche for adult neural stem cells. *Cell Stem*
1004 *Cell* **3**, 279-88 (2008).

1005 10. Doetsch, F., Garcia-Verdugo, J.M. & Alvarez-Buylla, A. Cellular composition and three-
1006 dimensional organization of the subventricular germinal zone in the adult mammalian
1007 brain. *J Neurosci* **17**, 5046-61 (1997).
1008 11. Kernie, S.G. & Parent, J.M. Forebrain neurogenesis after focal Ischemic and traumatic
1009 brain injury. *Neurobiol Dis* **37**, 267-74 (2010).
1010 12. Faiz, M. *et al.* Adult Neural Stem Cells from the Subventricular Zone Give Rise to
1011 Reactive Astrocytes in the Cortex after Stroke. *Cell Stem Cell* **17**, 624-34 (2015).
1012 13. Capilla-Gonzalez, V., Cebrian-Silla, A., Guerrero-Cazares, H., Garcia-Verdugo, J.M. &
1013 Quinones-Hinojosa, A. Age-related changes in astrocytic and ependymal cells of the
1014 subventricular zone. *Glia* **62**, 790-803 (2014).
1015 14. Enwere, E. *et al.* Aging results in reduced epidermal growth factor receptor signaling,
1016 diminished olfactory neurogenesis, and deficits in fine olfactory discrimination. *J*
1017 *Neurosci* **24**, 8354-65 (2004).
1018 15. Luo, J., Daniels, S.B., Lennington, J.B., Notti, R.Q. & Conover, J.C. The aging
1019 neurogenic subventricular zone. *Aging Cell* **5**, 139-52 (2006).
1020 16. Tropepe, V., Craig, C.G., Morshead, C.M. & van der Kooy, D. Transforming growth
1021 factor-alpha null and senescent mice show decreased neural progenitor cell proliferation
1022 in the forebrain subependyma. *J Neurosci* **17**, 7850-9 (1997).
1023 17. Klemm, S.L., Shipony, Z. & Greenleaf, W.J. Chromatin accessibility and the regulatory
1024 epigenome. *Nat Rev Genet* **20**, 207-220 (2019).
1025 18. Kane, A.E. & Sinclair, D.A. Epigenetic changes during aging and their reprogramming
1026 potential. *Crit Rev Biochem Mol Biol* **54**, 61-83 (2019).

1027 19. Gontier, G. *et al.* Tet2 Rescues Age-Related Regenerative Decline and Enhances
1028 Cognitive Function in the Adult Mouse Brain. *Cell Rep* **22**, 1974-1981 (2018).
1029 20. Martynoga, B. *et al.* Epigenomic enhancer annotation reveals a key role for NFIX in
1030 neural stem cell quiescence. *Genes Dev* **27**, 1769-86 (2013).
1031 21. Lupo, G. *et al.* Molecular profiling of aged neural progenitors identifies Dbx2 as a
1032 candidate regulator of age-associated neurogenic decline. *Aging Cell* **17**, e12745 (2018).
1033 22. Benayoun, B.A. *et al.* Remodeling of epigenome and transcriptome landscapes with
1034 aging in mice reveals widespread induction of inflammatory responses. *Genome Res* **29**,
1035 697-709 (2019).
1036 23. Shi, Z. *et al.* Single-cell transcriptomics reveals gene signatures and alterations associated
1037 with aging in distinct neural stem/progenitor cell subpopulations. *Protein Cell* **9**, 351-364
1038 (2018).
1039 24. Artegiani, B. *et al.* A Single-Cell RNA Sequencing Study Reveals Cellular and
1040 Molecular Dynamics of the Hippocampal Neurogenic Niche. *Cell Rep* **21**, 3271-3284
1041 (2017).
1042 25. Dulken, B.W. *et al.* Single-cell analysis reveals T cell infiltration in old neurogenic
1043 niches. *Nature* **571**, 205-210 (2019).
1044 26. Kalamakis, G. *et al.* Quiescence Modulates Stem Cell Maintenance and Regenerative
1045 Capacity in the Aging Brain. *Cell* **176**, 1407-1419 e14 (2019).
1046 27. Codega, P. *et al.* Prospective identification and purification of quiescent adult neural stem
1047 cells from their in vivo niche. *Neuron* **82**, 545-59 (2014).
1048 28. Leeman, D.S. *et al.* Lysosome activation clears aggregates and enhances quiescent neural
1049 stem cell activation during aging. *Science* **359**, 1277-1283 (2018).

1050 29. Buenrostro, J.D., Giresi, P.G., Zaba, L.C., Chang, H.Y. & Greenleaf, W.J. Transposition
1051 of native chromatin for fast and sensitive epigenomic profiling of open chromatin, DNA-
1052 binding proteins and nucleosome position. *Nat Methods* **10**, 1213-8 (2013).
1053 30. Ucar, D. *et al.* The chromatin accessibility signature of human immune aging stems from
1054 CD8(+) T cells. *J Exp Med* **214**, 3123-3144 (2017).
1055 31. Shcherbina, A. *et al.* Dissecting Murine Muscle Stem Cell Aging through Regeneration
1056 Using Integrative Genomic Analysis. *Cell Rep* **32**, 107964 (2020).
1057 32. Koohy, H. *et al.* Genome organization and chromatin analysis identify transcriptional
1058 downregulation of insulin-like growth factor signaling as a hallmark of aging in
1059 developing B cells. *Genome Biol* **19**, 126 (2018).
1060 33. Ge, Y. *et al.* The aging skin microenvironment dictates stem cell behavior. *Proc Natl*
1061 *Acad Sci U S A* **117**, 5339-5350 (2020).
1062 34. Guillemot, F. & Hassan, B.A. Beyond proneural: emerging functions and regulations of
1063 proneural proteins. *Curr Opin Neurobiol* **42**, 93-101 (2017).
1064 35. Shrikumar, A., Greenside, P. & Kundaje, A. Learning Important Features Through
1065 Propagating Activation Differences. in *Proceedings of the 34th International Conference*
1066 *on Machine Learning* Vol. 70 (eds Doina, P. & Yee Whye, T.) 3145--3153 (PMLR,
1067 Proceedings of Machine Learning Research, 2017).
1068 36. Avsec, Z. *et al.* Base-resolution models of transcription-factor binding reveal soft motif
1069 syntax. *Nat Genet* **53**, 354-366 (2021).
1070 37. Shrikumar, A. *et al.* Technical Note on Transcription Factor Motif Discovery from
1071 Importance Scores (TF-MoDISco) version 0.5.6.5. arXiv:1811.00416 (2018).

1072 38. Fane, M., Harris, L., Smith, A.G. & Piper, M. Nuclear factor one transcription factors as
1073 epigenetic regulators in cancer. *Int J Cancer* **140**, 2634-2641 (2017).
1074 39. Mira, H. *et al.* Signaling through BMPR-IA regulates quiescence and long-term activity
1075 of neural stem cells in the adult hippocampus. *Cell Stem Cell* **7**, 78-89 (2010).
1076 40. Jones, K.M. *et al.* CHD7 maintains neural stem cell quiescence and prevents premature
1077 stem cell depletion in the adult hippocampus. *Stem Cells* **33**, 196-210 (2015).
1078 41. Knobloch, M. *et al.* A Fatty Acid Oxidation-Dependent Metabolic Shift Regulates Adult
1079 Neural Stem Cell Activity. *Cell Rep* **20**, 2144-2155 (2017).
1080 42. Mizrahi, A., Lu, J., Irving, R., Feng, G. & Katz, L.C. In vivo imaging of juxtaglomerular
1081 neuron turnover in the mouse olfactory bulb. *Proc Natl Acad Sci U S A* **103**, 1912-7
1082 (2006).
1083 43. Gage, F.H. & Temple, S. Neural stem cells: generating and regenerating the brain.
1084 *Neuron* **80**, 588-601 (2013).
1085 44. Mobley, A.S. *et al.* Age-dependent regional changes in the rostral migratory stream.
1086 *Neurobiol Aging* **34**, 1873-81 (2013).
1087 45. Shuboni-Mulligan, D.D. *et al.* In vivo serial MRI of age-dependent neural progenitor cell
1088 migration in the rat brain. *Neuroimage* **199**, 153-159 (2019).
1089 46. Capilla-Gonzalez, V., Cebrian-Silla, A., Guerrero-Cazares, H., Garcia-Verdugo, J.M. &
1090 Quinones-Hinojosa, A. The generation of oligodendroglial cells is preserved in the rostral
1091 migratory stream during aging. *Front Cell Neurosci* **7**, 147 (2013).
1092 47. Fritze, J. *et al.* Loss of Cxcr5 alters neuroblast proliferation and migration in the aged
1093 brain. *Stem Cells* **38**, 1175-1187 (2020).

1094 48. Morante-Redolat, J.M. & Porlan, E. Neural Stem Cell Regulation by Adhesion Molecules
1095 Within the Subependymal Niche. *Front Cell Dev Biol* **7**, 102 (2019).
1096 49. Tario, J.D., Jr., Conway, A.N., Muirhead, K.A. & Wallace, P.K. Monitoring Cell
1097 Proliferation by Dye Dilution: Considerations for Probe Selection. *Methods Mol Biol*
1098 **1678**, 249-299 (2018).
1099 50. Molofsky, A.V. *et al.* Increasing p16INK4a expression decreases forebrain progenitors
1100 and neurogenesis during ageing. *Nature* **443**, 448-52 (2006).
1101 51. Ahlenius, H., Visan, V., Kokaia, M., Lindvall, O. & Kokaia, Z. Neural stem and
1102 progenitor cells retain their potential for proliferation and differentiation into functional
1103 neurons despite lower number in aged brain. *J Neurosci* **29**, 4408-19 (2009).
1104 52. Blanchoin, L., Boujemaa-Paterski, R., Sykes, C. & Plastino, J. Actin dynamics,
1105 architecture, and mechanics in cell motility. *Physiol Rev* **94**, 235-63 (2014).
1106 53. Thomas, C. Bundling actin filaments from membranes: some novel players. *Front Plant*
1107 *Sci* **3**, 188 (2012).
1108 54. Morimatsu, M., Mekhdjian, A.H., Adhikari, A.S. & Dunn, A.R. Molecular tension
1109 sensors report forces generated by single integrin molecules in living cells. *Nano Lett* **13**,
1110 3985-9 (2013).
1111 55. Chang, A.C. *et al.* Single Molecule Force Measurements in Living Cells Reveal a
1112 Minimally Tensioned Integrin State. *ACS Nano* **10**, 10745-10752 (2016).
1113 56. Suzuki, N., Hajicek, N. & Kozasa, T. Regulation and physiological functions of G12/13-
1114 mediated signaling pathways. *Neurosignals* **17**, 55-70 (2009).
1115 57. Amano, M., Nakayama, M. & Kaibuchi, K. Rho-kinase/ROCK: A key regulator of the
1116 cytoskeleton and cell polarity. *Cytoskeleton (Hoboken)* **67**, 545-54 (2010).

1117 58. Burridge, K. & Wennerberg, K. Rho and Rac take center stage. *Cell* **116**, 167-79 (2004).
1118 59. Christie, K.J., Turbic, A. & Turnley, A.M. Adult hippocampal neurogenesis, Rho kinase
1119 inhibition and enhancement of neuronal survival. *Neuroscience* **247**, 75-83 (2013).
1120 60. Emre, N. *et al.* The ROCK inhibitor Y-27632 improves recovery of human embryonic
1121 stem cells after fluorescence-activated cell sorting with multiple cell surface markers.
1122 *PLoS One* **5**, e12148 (2010).
1123 61. Ishizaki, T. *et al.* Pharmacological properties of Y-27632, a specific inhibitor of rho-
1124 associated kinases. *Mol Pharmacol* **57**, 976-83 (2000).
1125 62. Uehata, M. *et al.* Calcium sensitization of smooth muscle mediated by a Rho-associated
1126 protein kinase in hypertension. *Nature* **389**, 990-4 (1997).
1127 63. Kim, J.E., Ryu, H.J., Kim, M.J. & Kang, T.C. LIM kinase-2 induces programmed
1128 necrotic neuronal death via dysfunction of DRP1-mediated mitochondrial fission. *Cell*
1129 *Death Differ* **21**, 1036-49 (2014).
1130 64. Leong, S.Y., Faux, C.H., Turbic, A., Dixon, K.J. & Turnley, A.M. The Rho kinase
1131 pathway regulates mouse adult neural precursor cell migration. *Stem Cells* **29**, 332-43
1132 (2011).
1133 65. Peh, G.S. *et al.* The effects of Rho-associated kinase inhibitor Y-27632 on primary
1134 human corneal endothelial cells propagated using a dual media approach. *Sci Rep* **5**, 9167
1135 (2015).
1136 66. Narumiya, S., Ishizaki, T. & Uehata, M. Use and properties of ROCK-specific inhibitor
1137 Y-27632. *Methods Enzymol* **325**, 273-84 (2000).
1138 67. Tumpel, S. & Rudolph, K.L. Quiescence: Good and Bad of Stem Cell Aging. *Trends Cell*
1139 *Biol* **29**, 672-685 (2019).

1140 68. Liu, L. *et al.* Chromatin modifications as determinants of muscle stem cell quiescence
1141 and chronological aging. *Cell Rep* **4**, 189-204 (2013).
1142 69. Schworer, S. *et al.* Epigenetic stress responses induce muscle stem-cell ageing by Hoxa9
1143 developmental signals. *Nature* **540**, 428-432 (2016).
1144 70. Sun, D. *et al.* Epigenomic profiling of young and aged HSCs reveals concerted changes
1145 during aging that reinforce self-renewal. *Cell Stem Cell* **14**, 673-88 (2014).
1146 71. Bock, C. *et al.* DNA methylation dynamics during in vivo differentiation of blood and
1147 skin stem cells. *Mol Cell* **47**, 633-47 (2012).
1148 72. Beerman, I. *et al.* Proliferation-dependent alterations of the DNA methylation landscape
1149 underlie hematopoietic stem cell aging. *Cell Stem Cell* **12**, 413-25 (2013).
1150 73. Mauffrey, P. *et al.* Progenitors from the central nervous system drive neurogenesis in
1151 cancer. *Nature* **569**, 672-678 (2019).
1152 74. Miroshnikova, Y.A., Nava, M.M. & Wickstrom, S.A. Emerging roles of mechanical
1153 forces in chromatin regulation. *J Cell Sci* **130**, 2243-2250 (2017).
1154 75. Nava, M.M. *et al.* Heterochromatin-Driven Nuclear Softening Protects the Genome
1155 against Mechanical Stress-Induced Damage. *Cell* **181**, 800-817 e22 (2020).
1156 76. Segel, M. *et al.* Niche stiffness underlies the ageing of central nervous system progenitor
1157 cells. *Nature* **573**, 130-134 (2019).
1158 77. Goetsch, K.P., Snyman, C., Myburgh, K.H. & Niesler, C.U. ROCK-2 is associated with
1159 focal adhesion maturation during myoblast migration. *J Cell Biochem* **115**, 1299-307
1160 (2014).
1161 78. Salhia, B. *et al.* Inhibition of Rho-kinase affects astrocytoma morphology, motility, and
1162 invasion through activation of Rac1. *Cancer Res* **65**, 8792-800 (2005).

1163 79. Chen, Y., Chou, W.C., Ding, Y.M. & Wu, Y.C. Caffeine inhibits migration in glioma
1164 cells through the ROCK-FAK pathway. *Cell Physiol Biochem* **33**, 1888-98 (2014).
1165 80. Fu, P.C. *et al.* The Rho-associated kinase inhibitors Y27632 and fasudil promote
1166 microglial migration in the spinal cord via the ERK signaling pathway. *Neural Regen Res*
1167 **13**, 677-683 (2018).
1168 81. Piltti, J., Varjosalo, M., Qu, C., Hayrinen, J. & Lammi, M.J. Rho-kinase inhibitor Y-
1169 27632 increases cellular proliferation and migration in human foreskin fibroblast cells.
1170 *Proteomics* **15**, 2953-65 (2015).
1171 82. Rudolph, J. *et al.* The JAK inhibitor ruxolitinib impairs dendritic cell migration via off-
1172 target inhibition of ROCK. *Leukemia* **30**, 2119-2123 (2016).
1173 83. Srinivasan, S. *et al.* Blockade of ROCK inhibits migration of human primary
1174 keratinocytes and malignant epithelial skin cells by regulating actomyosin contractility.
1175 *Sci Rep* **9**, 19930 (2019).
1176 84. Dyberg, C. *et al.* Inhibition of Rho-Associated Kinase Suppresses Medulloblastoma
1177 Growth. *Cancers (Basel)* **12**(2019).
1178 85. Feng, J.F. *et al.* Guided migration of neural stem cells derived from human embryonic
1179 stem cells by an electric field. *Stem Cells* **30**, 349-55 (2012).
1180 86. Koch, J.C. *et al.* ROCK inhibition in models of neurodegeneration and its potential for
1181 clinical translation. *Pharmacol Ther* **189**, 1-21 (2018).
1182 87. Zhuo, L. *et al.* Live astrocytes visualized by green fluorescent protein in transgenic mice.
1183 *Dev Biol* **187**, 36-42 (1997).

1184 88. Shen, L., Shao, N., Liu, X. & Nestler, E. ngs.plot: Quick mining and visualization of
1185 next-generation sequencing data by integrating genomic databases. *BMC Genomics* **15**,
1186 284 (2014).
1187 89. Stark, R.B., G.D. DiffBind: differential binding analysis of ChIP-seq peak data.
1188 *Bioconductor* (2011).
1189 90. Ross-Innes, C.S. *et al.* Differential oestrogen receptor binding is associated with clinical
1190 outcome in breast cancer. *Nature* **481**, 389-93 (2012).
1191 91. Yu, G., Wang, L.G. & He, Q.Y. ChIPseeker: an R/Bioconductor package for ChIP peak
1192 annotation, comparison and visualization. *Bioinformatics* **31**, 2382-3 (2015).
1193 92. Love, M.I., Huber, W. & Anders, S. Moderated estimation of fold change and dispersion
1194 for RNA-seq data with DESeq2. *Genome Biol* **15**, 550 (2014).
1195 93. Robinson, M.D., McCarthy, D.J. & Smyth, G.K. edgeR: a Bioconductor package for
1196 differential expression analysis of digital gene expression data. *Bioinformatics* **26**, 139-40
1197 (2010).
1198 94. McCarthy, D.J., Chen, Y. & Smyth, G.K. Differential expression analysis of multifactor
1199 RNA-Seq experiments with respect to biological variation. *Nucleic Acids Res* **40**, 4288-
1200 97 (2012).
1201 95. Schep, A.N. *et al.* Structured nucleosome fingerprints enable high-resolution mapping of
1202 chromatin architecture within regulatory regions. *Genome Res* **25**, 1757-70 (2015).
1203 96. Chen, E.Y. *et al.* Enrichr: interactive and collaborative HTML5 gene list enrichment
1204 analysis tool. *BMC Bioinformatics* **14**, 128 (2013).
1205 97. Kuleshov, M.V. *et al.* Enrichr: a comprehensive gene set enrichment analysis web server
1206 2016 update. *Nucleic Acids Res* **44**, W90-7 (2016).

1207 98. Heinz, S. *et al.* Simple combinations of lineage-determining transcription factors prime
1208 cis-regulatory elements required for macrophage and B cell identities. *Mol Cell* **38**, 576-
1209 89 (2010).
1210 99. Kelley, D.R., Snoek, J. & Rinn, J.L. Basset: learning the regulatory code of the accessible
1211 genome with deep convolutional neural networks. *Genome Res* **26**, 990-9 (2016).
1212 100. Stuart, T. *et al.* Comprehensive Integration of Single-Cell Data. *Cell* **177**, 1888-1902 e21
1213 (2019).
1214 101. Kramer, A., Green, J., Pollard, J., Jr. & Tugendreich, S. Causal analysis approaches in
1215 Ingenuity Pathway Analysis. *Bioinformatics* **30**, 523-30 (2014).
1216 102. Schindelin, J. *et al.* Fiji: an open-source platform for biological-image analysis. *Nat*
1217 *Methods* **9**, 676-82 (2012).
1218 103. Tan, S.J. *et al.* Regulation and dynamics of force transmission at individual cell-matrix
1219 adhesion bonds. *Sci Adv* **6**, eaax0317 (2020).
1220 104. Morimatsu, M., Mekhdjian, A.H., Chang, A.C., Tan, S.J. & Dunn, A.R. Visualizing the
1221 interior architecture of focal adhesions with high-resolution traction maps. *Nano Lett* **15**,
1222 2220-8 (2015).
1223 105. Edelstein, A.D. *et al.* Advanced methods of microscope control using muManager
1224 software. *J Biol Methods* **1**(2014).
1225
1226
1227

Figure 1

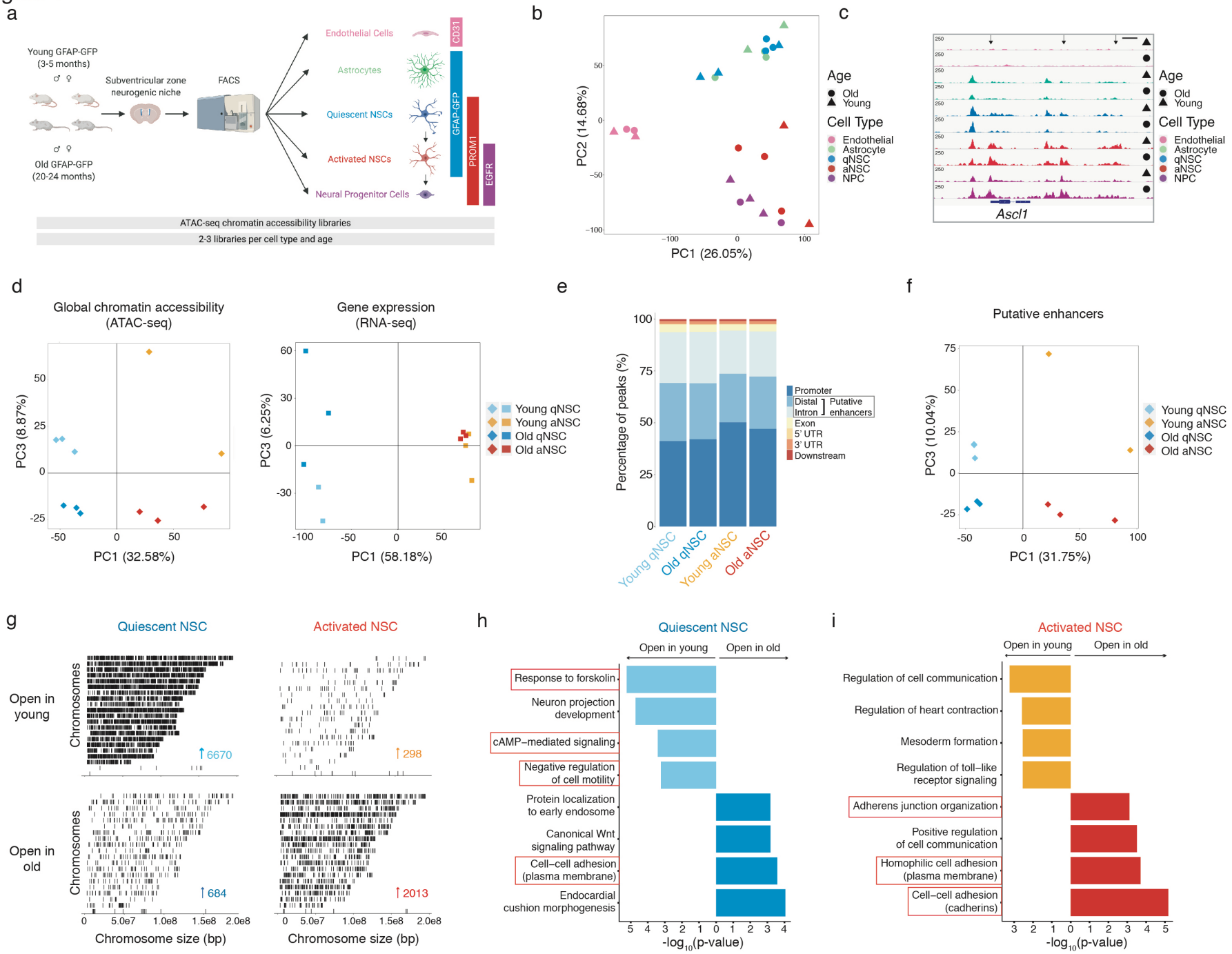
a
Young GFAP-GFP
(3-5 months)
Subventricular zone
neurogenic niche
FACS
Old GFAP-GFP
(20-24 months)
Endothelial Cells
Astrocytes
Quiescent NSCs
Activated NSCs
Neural Progenitor Cells
CD31
GFAP-GFP
PROM1
EGFR
ATAC-seq chromatin accessibility libraries
2-3 libraries per cell type and age
b
PC2 (14.68%)
PC1 (26.05%)
Age
Old
Young
Cell Type
Endothelial
Astrocyte
qNSC
aNSC
NPC
c
Ascl1
Age
Old
Young
Cell Type
Endothelial
Astrocyte
qNSC
aNSC
NPC
d
Global chromatin accessibility
(ATAC-seq)
PC3 (8.87%)
PC1 (32.58%)
Gene expression
(RNA-seq)
PC3 (6.25%)
PC1 (58.18%)
Young qNSC
Young aNSC
Old qNSC
Old aNSC
e
Percentage of peaks (%)
Promoter
Distal
Intron
Putative enhancers
Exon
5' UTR
3' UTR
Downstream
Young qNSC
Old qNSC
Young aNSC
Old aNSC
f
Putative enhancers
PC3 (10.04%)
PC1 (31.75%)
Young qNSC
Young aNSC
Old qNSC
Old aNSC
g
Quiescent NSC
Activated NSC
Open in young
Open in old
Chromosomes
6670
298
684
2013
Chromosome size (bp)
h
Quiescent NSC
Open in young
Open in old
Response to forskolin
Neuron projection development
cAMP–mediated signaling
Negative regulation of cell motility
Protein localization to early endosome
Canonical Wnt signaling pathway
Cell–cell adhesion (plasma membrane)
Endocardial cushion morphogenesis
-log10(p-value)
i
Activated NSC
Open in young
Open in old
Regulation of cell communication
Regulation of heart contraction
Mesoderm formation
Regulation of toll–like receptor signaling
Adherens junction organization
Positive regulation of cell communication
Homophilic cell adhesion (plasma membrane)
Cell–cell adhesion (cadherins)
-log10(p-value)

1228 **Figure 1: The chromatin landscape of five cell types in the SVZ neurogenic region reveals**
1229 **opposing chromatin changes with age in quiescent and activated NSCs involving cell**
1230 **adhesion and migration pathways**
1231
1232 **a)** Experimental design for freshly isolating cells from the subventricular zone (SVZ)
1233 neurogenic niche in young (3-5 months) and old (20-24 months) GFAP-GFP mice. For each
1234 library, 800-2000 cells were pooled from male and female GFAP-GFP mice using
1235 fluorescence-activated cell sorted (FACS) (see Methods). NSC: neural stem cell. GFAP,
1236 Glial Fibrillary Acidic Protein. PROM1, Prominin-1. EGFR, epidermal growth factor
1237 receptor.
1238 **b)** Principal Component Analysis (PCA) on all chromatin peaks from endothelial cells,
1239 astrocytes, quiescent NSCs (qNSCs), activated NSCs (aNSCs), and neural progenitor cells
1240 (NPCs) freshly isolated from the SVZ of young (triangle) and old (round) GFAP-GFP mice
1241 where each dot represents a single ATAC-seq library. PCA was generated using the variance
1242 stabilizing transformation (VST)-normalized global consensus count matrix. PC, principal
1243 component.
1244 **c)** Genome browser (IGV) view of chromatin accessibility signal tracks from representative
1245 RPKM-normalized libraries of all SVZ niche cell types around the *Ascl1* loci. Black arrows
1246 represent sites of differentially accessible peaks that open in young aNSCs when compared to
1247 young qNSCs. *Ascl1*, Achaete-Scute Family bHLH Transcription Factor 1. Scale bar, 1kb.
1248 **d)** PCA on all genome-wide chromatin peaks (left) and mRNA gene expression[28] (right) from
1249 qNSCs and aNSCs freshly isolated from the young and old SVZ where each dot represents a
1250 single sequencing library (PC1 vs. PC3). ATAC-seq libraries are represented by diamonds

1251 and RNA-seq libraries are represented by squares. PCAs were both generated using variance
1252 stabilizing transformation (VST)-normalized read counts. PC, principal component.
1253 **e)** Bar graph representing the genomic distribution of open chromatin peaks for qNSCs and
1254 aNSCs in young and old conditions based on their pooled peaksets. ATAC-seq peaks were
1255 annotated with ChIPSeeker (v1.18.0). Grey box indicates distal and intronic peaks that likely
1256 contain putative enhancers.
1257 **f)** PCA on putative enhancers (exclusively distal/intronic chromatin peaks) from qNSCs and
1258 aNSCs freshly isolated from the young and old SVZ where each dot represents a single
1259 ATAC-seq library (PC1 vs. PC3). PCA was generated using the variance stabilizing
1260 transformation (VST)-normalized NSC consensus count matrix. PC, principal component.
1261 **g)** Chromosome-level visualization of differentially accessible ATAC-seq peaks (FDR<0.05)
1262 that change with age in qNSCs (left) and aNSCs (right) respectively. Each vertical bar
1263 represents a dynamic ATAC-seq peak aligned to mouse chromosomes (*mm10* version of the
1264 mouse genome) that is differentially open in young (top) or old (bottom) NSCs.
1265 **h,i)** Selected GO terms for genes associated with differentially accessible ATAC-seq peaks
1266 (FDR<0.05) that change with age in quiescent (h) and activated (i) NSCs generated by
1267 EnrichR and ranked by *P*-value. ATAC-seq peaks were annotated with their nearest gene
1268 using ChIPSeeker (v1.18.0). Red boxes indicate GO terms associated with adhesion and
1269 migration.
1270
1271
1272

Figure 2

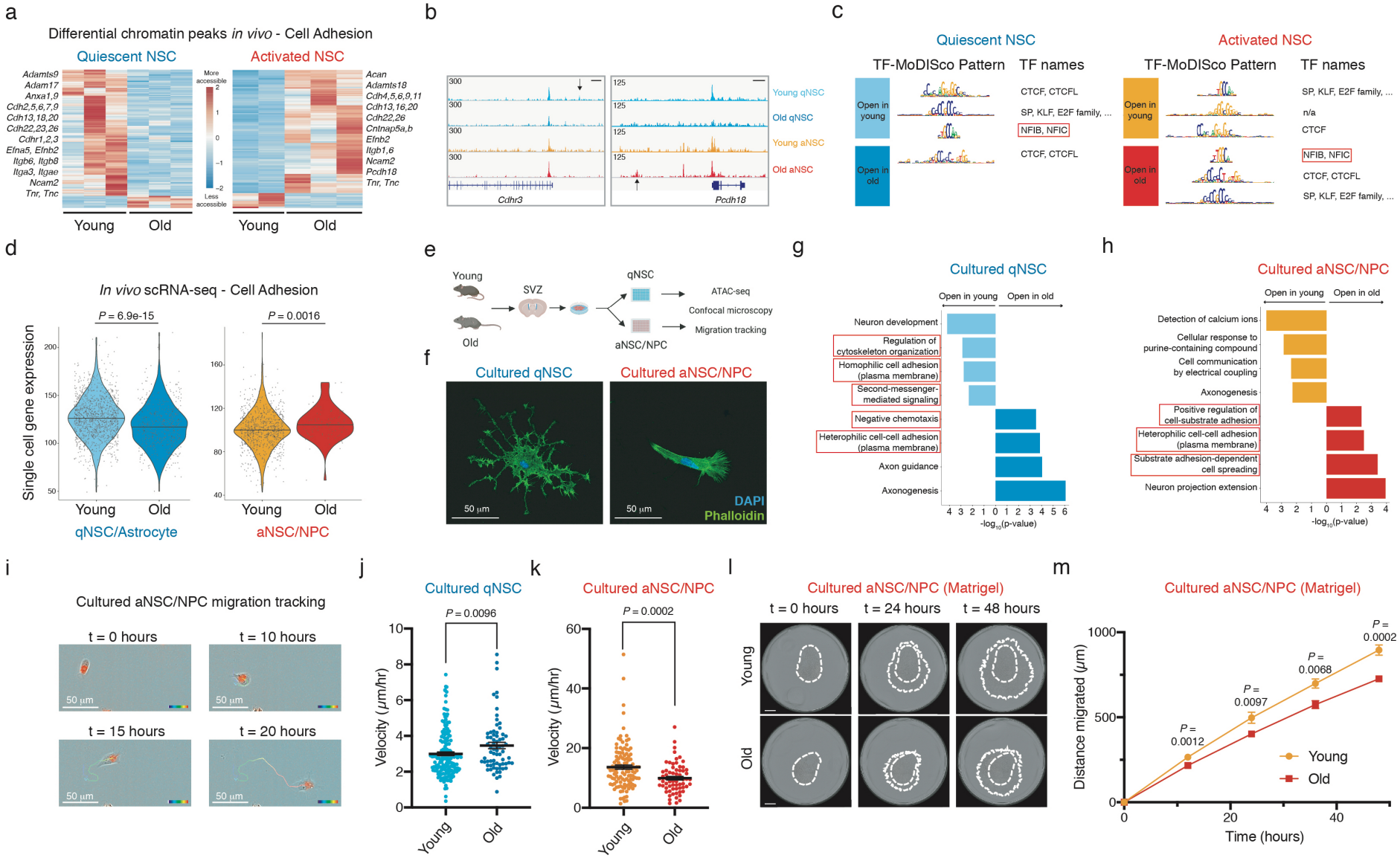
a
Differential chromatin peaks in vivo - Cell Adhesion
Quiescent NSC
Activated NSC
Young
Old
b
Cdhr3
Pcdh18
Young qNSC
Old qNSC
Young aNSC
Old aNSC
c
Quiescent NSC
Activated NSC
TF-MoDISco Pattern
TF names
Open in young
Open in old
d
In vivo scRNA-seq - Cell Adhesion
P = 6.9e-15
P = 0.0016
Single cell gene expression
qNSC/Astrocyte
aNSC/NPC
e
Young
Old
SVZ
qNSC
aNSC/NPC
ATAC-seq
Confocal microscopy
Migration tracking
f
Cultured qNSC
Cultured aNSC/NPC
50 µm
DAPI
Phalloidin
g
Cultured qNSC
Open in young
Open in old
Neuron development
Regulation of cytoskeleton organization
Homophilic cell adhesion (plasma membrane)
Second-messenger-mediated signaling
Negative chemotaxis
Heterophilic cell-cell adhesion (plasma membrane)
Axon guidance
Axonogenesis
-log10(p-value)
h
Cultured aNSC/NPC
Detection of calcium ions
Cellular response to purine-containing compound
Cell communication by electrical coupling
Axonogenesis
Positive regulation of cell-substrate adhesion
Heterophilic cell-cell adhesion (plasma membrane)
Substrate adhesion-dependent cell spreading
Neuron projection extension
i
Cultured aNSC/NPC migration tracking
t = 0 hours
t = 10 hours
t = 15 hours
t = 20 hours
50 µm
j
Cultured qNSC
P = 0.0096
Velocity (µm/hr)
Young
Old
k
Cultured aNSC/NPC
P = 0.0002
l
Cultured aNSC/NPC (Matrigel)
t = 0 hours
t = 24 hours
t = 48 hours
m
Cultured aNSC/NPC (Matrigel)
Distance migrated (µm)
Time (hours)
P = 0.0012
P = 0.0097
P = 0.0068
P = 0.0002

1273 **Figure 2: The opposing chromatin changes in old quiescent and activated NSCs with aging**
1274 **are associated with functional defects in cell adhesion and migration**
1275
1276 **a)** Heatmap showing accessibility levels of differential ATAC-seq peaks associated with the
1277 "Cell Adhesion" GO category (GO:0007155) that change with age in qNSCs (left) and
1278 aNSCs (right) respectively. Selected gene names with associated differentially accessible
1279 peaks are displayed. TMM-normalized read counts (by EdgeR), scaled row-wise.
1280 **b)** Genome browser (IGV) view of chromatin accessibility signal tracks from representative
1281 RPKM-normalized libraries of quiescent and activated NSCs isolated from young and old
1282 brains illustrating differential chromatin peaks that change with age in young quiescent NSCs
1283 (left) and old activated NSCs (right) respectively. Black arrows represent sites of
1284 differentially accessible peaks that change with age in qNSCs (left) and aNSCs (right)
1285 respectively. *Cdhr3*, Cadherin Related Family Member 3. *Pcdh18*, Protocadherin 18. Scale
1286 bar, 5kb.
1287 **c)** Enrichment of top-ranked transcription factor motifs by TF-MoDISco within differentially
1288 accessible ATAC-seq peaks that change with age in qNSCs (left) and aNSCs (right). Red box
1289 indicates motif associated with NFI family.
1290 **d)** Violin plots of the average distribution of single cell cumulative expression profiles of genes
1291 within the "Cell Adhesion" GO category (GO:0007155) for young and old qNSCs/astrocytes
1292 (left) and aNSCs/NPCs (right) from scRNA-seq data[25]. Each overlaid dot represents the
1293 cumulative expression of cell adhesion genes in a single cell. *P*-values were calculated using
1294 a two-tailed Mann-Whitney test.

1295 **e)** Schematic illustrating the general protocol for experiments involving cultured qNSCs and
1296 aNSCs/NPCs. Young (3-5 months) and old (20-24 months) C57BL/6 SVZs were
1297 microdissected and tissues were processed to enable NSC culture. Quiescence was induced
1298 with growth factors bFGF and BMP4 for 5-10 days, and activation was maintained with
1299 bFGF and EGF for 1-2 days prior to downstream experiments (ATAC-seq library generation,
1300 confocal microscopy, and live-cell migration tracking).
1301 **f)** Representative images of immunofluorescence staining of a young (3 months) qNSC (left)
1302 and aNSC/NPC (right) cultured on Poly-D-Lysine. Blue, DAPI (nuclei); green, phalloidin (F-
1303 actin). Scale bar, 50 μm.
1304 **g,h)** Selected GO terms for genes associated with differentially accessible ATAC-seq peaks
1305 (FDR<0.05) that change with age in cultured qNSCs (g) and aNSCs/NPCs (h) generated by
1306 EnrichR and ranked by *P*-value. Red boxes indicate GO terms associated with cell adhesion
1307 and cell migration.
1308 **i)** Representative images of a young (3-4 months) aNSC/NPC in the presence of cell-permeant
1309 red fluorescent nucleic acid stain Syto64 taken at t = 0, 10, 15, and 20 hours after sorting
1310 onto Poly-D-Lysine. The Incucyte system was used for 20x imaging and migration tracks
1311 were determined using Imaris (v9.3.0). Color gradient bar represents the passage of time
1312 from 0 (blue) to 20 (red) hours. Scale bar, 50 μm.
1313 **j)** Migration speed of young (3-4 months) and old (23-24 months) qNSCs on Poly-D-Lysine.
1314 Each dot represents the average velocity of a single cell over a 20-hour period (n = 6 young
1315 male mice, and n = 4 old male mice) (combined over 2 experiments). Data are mean ± SEM.
1316 *P*-values were calculated using a two-tailed Mann-Whitney test.

1317 **k)** Migration speed of young (3-4 months) and old (21-24 months) aNSCs/NPCs on Poly-D-
1318 Lysine. Each dot represents the average velocity of a single cell over a 20-hour period (*n* = 9
1319 young male mice, and *n* = 7 old male mice) (combined over 3 experiments). Data are mean ±
1320 SEM. *P*-values were calculated using a two-tailed Mann-Whitney test.
1321 **l)** Representative images of young (top) and old (bottom) aNSC/NPC invasion through
1322 Matrigel taken 0, 24, and 48 hours after seeding aNSCs/NPCs. The dotted white outline
1323 represents the outermost extent of invasion and the inner dotted white line represents the
1324 initial extent of the cells after seeding (t = 0 hours). Scale bar, 800 μm.
1325 **m)** Migration distance timecourse of young (3-4 months) and old (21-24 months) aNSC/NPC
1326 invasion through Matrigel over 48 hours with 12-hour intervals. (*n* = 7 young male mice, and
1327 *n* = 10 old male mice) (combined over 2 experiments). For each biological replicate, 1-4
1328 technical replicates were evaluated, and migration distance was averaged at each timepoint.
1329 Data are mean ± SEM. *P*-values were calculated at each timepoint using a two-tailed Mann-
1330 Whitney test.
1331
1332
1333
1334
1335
1336
1337
1338

Figure 3

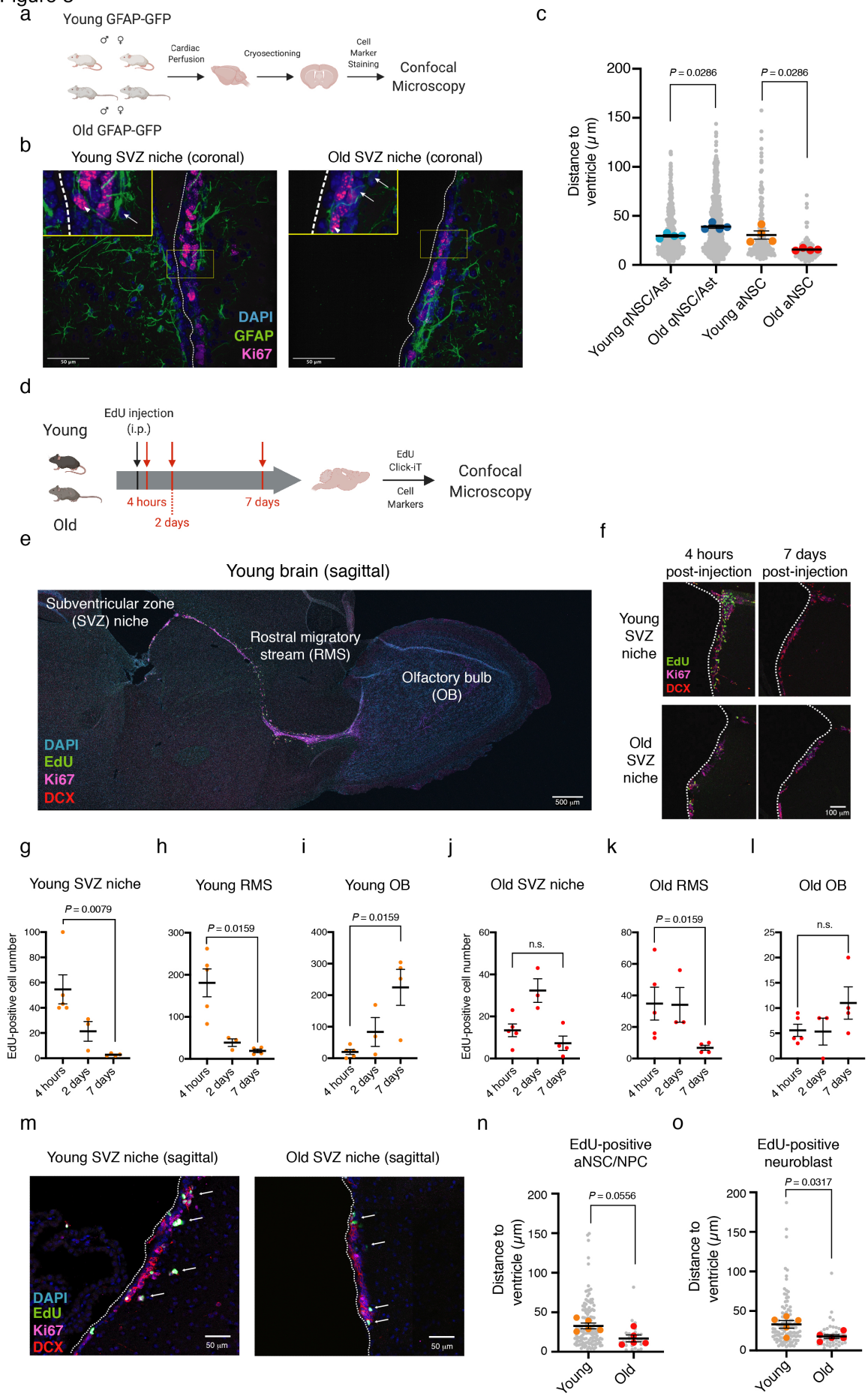
a
Young GFAP-GFP
Cardiac Perfusion
Cryosectioning
Cell Marker Staining
Confocal Microscopy
Old GFAP-GFP
b
Young SVZ niche (coronal)
Old SVZ niche (coronal)
DAPI
GFAP
Ki67
c
Distance to ventricle (μm)
P = 0.0286
P = 0.0286
Young qNSC/Ast
Old qNSC/Ast
Young aNSC
Old aNSC
d
Young
Old
EdU injection (i.p.)
4 hours
2 days
7 days
EdU Click-iT
Cell Markers
Confocal Microscopy
e
Young brain (sagittal)
Subventricular zone (SVZ) niche
Rostral migratory stream (RMS)
Olfactory bulb (OB)
DAPI
EdU
Ki67
DCX
500 μm
f
4 hours post-injection
7 days post-injection
Young SVZ niche
Old SVZ niche
EdU
Ki67
DCX
100 μm
g
Young SVZ niche
P = 0.0079
h
Young RMS
P = 0.0159
i
Young OB
P = 0.0159
j
Old SVZ niche
n.s.
k
Old RMS
P = 0.0159
l
Old OB
n.s.
EdU-positive cell number
4 hours
2 days
7 days
m
Young SVZ niche (sagittal)
Old SVZ niche (sagittal)
DAPI
EdU
Ki67
DCX
50 μm
n
EdU-positive aNSC/NPC
P = 0.0556
Distance to ventricle (μm)
Young
Old
o
EdU-positive neuroblast
P = 0.0317
Distance to ventricle (μm)
Young
Old

1339 **Figure 3: Age-dependent cell adhesion and migration defects of quiescent and activated**

1340 **NSCs and progenitors *in vivo***

1341

1342 **a)** Design of immunofluorescence experiments for quantifying the localization of

1343 qNSCs/astrocytes and aNSCs *in vivo* during aging in coronal brain sections. Young (4

1344 months) and old (18-26 months) mixed-sex GFAP-GFP animals were perfused with 4%

1345 PFA, brains were cryosectioned at a thickness of 16 μm and stained for cell markers prior to

1346 quantification with confocal microscopy.

1347 **b)** Representative images of immunofluorescence staining of coronal SVZ sections from young

1348 (4 months) (left) and old (18-26 months) (right) GFAP-GFP brains. Yellow box denotes inset

1349 containing qNSCs/astrocytes (GFAP+/Ki67-) and aNSCs (GFAP+/Ki67+) indicated with

1350 white arrows and arrowheads, respectively. The ventricular lining is indicated by a dotted

1351 white line. Blue, DAPI (nuclei); green, GFAP (Astrocyte/NSC marker); pink, Ki67

1352 (proliferation marker). Scale bar, 50 μm.

1353 **c)** NSC distance to the ventricle was calculated for qNSCs/astrocytes (GFAP+/Ki67-) and

1354 aNSCs (GFAP+/Ki67+) in coronal sections of young (4 months) and old (18-26 months)

1355 SVZs. Each gray dot represents the distance of a single cell from the ventricular lining and

1356 each colored dot represents the mean distance from the ventricle per animal (n = 4 mixed-sex

1357 young mice, and n = 4 mixed-sex old mice) (combined over 4 paired young/old experiments).

1358 Data are mean ± SEM. Ast, astrocytes. P-values were calculated using a two-tailed Mann-

1359 Whitney test comparing sample means between conditions.

1360 **d)** Design of immunofluorescence experiments to assess EdU-labelled NSC migration out of the

1361 SVZ *in vivo*. Young (2-3 months) and old (21 months) C57/BL6 male animals were

1362 intraperitoneally injected with EdU, and then sacrificed and perfused with 4% PFA after a
1363 time interval of 4 hours, 2 days, or 7 days. Perfused brains were sagittally cryosectioned at a
1364 thickness of 16 μm and stained for EdU and cell markers prior to quantification with
1365 confocal microscopy. EdU, 5-Ethynyl-2'-deoxyuridine. I.p., intraperitoneal.

1366 **e)** Representative immunofluorescence staining of sagittal sections encompassing the
1367 subventricular zone (SVZ) niche, rostral migratory stream (RMS), and olfactory bulb (OB) of
1368 a young (2-3 months) male C57BL/6 mouse 4hrs after intraperitoneal EdU injection. Blue,
1369 DAPI (nuclei); green, EdU (proliferation marker); pink, Ki67 (aNSC/NPC/neuroblast
1370 marker); red, DCX (neuroblast marker). Scale bar, 500 μm.

1371 **f)** Representative image of immunofluorescence staining in sagittal sections of the SVZ niche
1372 from a young (2-3 months) (top) or old (21 months) (bottom) male C57BL/6 mouse 4hrs
1373 (left) or 7 days (right) after intraperitoneal EdU injection. The ventricular lining is indicated
1374 by a dotted white line. Green, EdU (proliferation marker); pink, Ki67 (aNSC/NPC/neuroblast
1375 marker); red, DCX (neuroblast marker). Scale bar, 100 μm.

1376**g,h,i)** Quantification of EdU+ cells counted in the SVZ (g), RMS (h), and OB (i) from young (2-3
1377 months) sagittal sections 4 hours, 2 days, and 7 days post-injection of EdU. Each colored dot
1378 represents the number of EdU+ cells counted in a sagittal section from a single animal (n = 5
1379 young male mice 4 hours post-injection, n = 3 young male mice 2 days post-injection, n = 4
1380 young male mice 7 days post-injection) (combined over 2 experiment). Data are mean ±
1381 SEM. P-values were calculated using a two-tailed Mann-Whitney test.

1382**j,k,l)** Quantification of EdU+ cells counted in the SVZ (j), RMS (k), and OB (l) from old (21
1383 months) sagittal sections 4 hours, 2 days, and 7 days post-injection of EdU. Each colored dot
1384 represents the number of EdU+ cells counted in a sagittal section from a single animal (n = 5

1385 old male mice 4 hours post-injection, *n* = 3 old male mice 2 days post-injection, *n* = 4 old
1386 male mice 7 days post-injection) (combined over 2 experiment). Data are mean ± SEM. *P*-
1387 values were calculated using a two-tailed Mann-Whitney test.

1388 **m)** Representative images of immunofluorescence staining of sagittal SVZ sections of young (2-
1389 3 months) (left) and old (21 months) (right) male C57BL/6 mice 4hrs after intraperitoneal
1390 EdU injection. Blue, DAPI (nuclei); green, EdU (proliferation marker); pink, Ki67
1391 (aNSC/NPC/neuroblast marker); red, DCX (neuroblast marker). Dotted white line indicates
1392 ventricle wall and white arrows indicate selected EdU-positive cells. Scale bar, 50 μm.

1393 **n)** Distance to the ventricle was calculated for EdU+ aNSCs/NPCs (Ki67+/DCX-) in sagittal
1394 sections of young (2-3 months) and old (21 months) SVZs 4 hours after EdU injection. Each
1395 gray dot represents the distance of a single aNSC/NPC from the ventricle and each colored
1396 dot represents the mean aNSC/NPC distance from the ventricle per animal (*n* = 5 young male
1397 mice, and *n* = 5 old male mice) (combined over 2 experiments). Data are mean ± SEM. *P*-
1398 values were calculated using a two-tailed Mann-Whitney test comparing sample means
1399 between conditions.

1400 **o)** Distance to the ventricle was calculated for EdU+ neuroblasts (DCX+) in sagittal sections of
1401 young (2-3 months) and old (21 months) SVZs 4 hours after EdU injection. Each gray dot
1402 represents the distance of a single neuroblast from the ventricle and each colored dot
1403 represents the mean neuroblast distance from the ventricle per animal (*n* = 5 young male
1404 mice, and *n* = 5 old male mice) (combined over 2 experiments). Data are mean ± SEM. *P*-
1405 values were calculated using a two-tailed Mann-Whitney test comparing sample means
1406 between conditions.

Figure 4

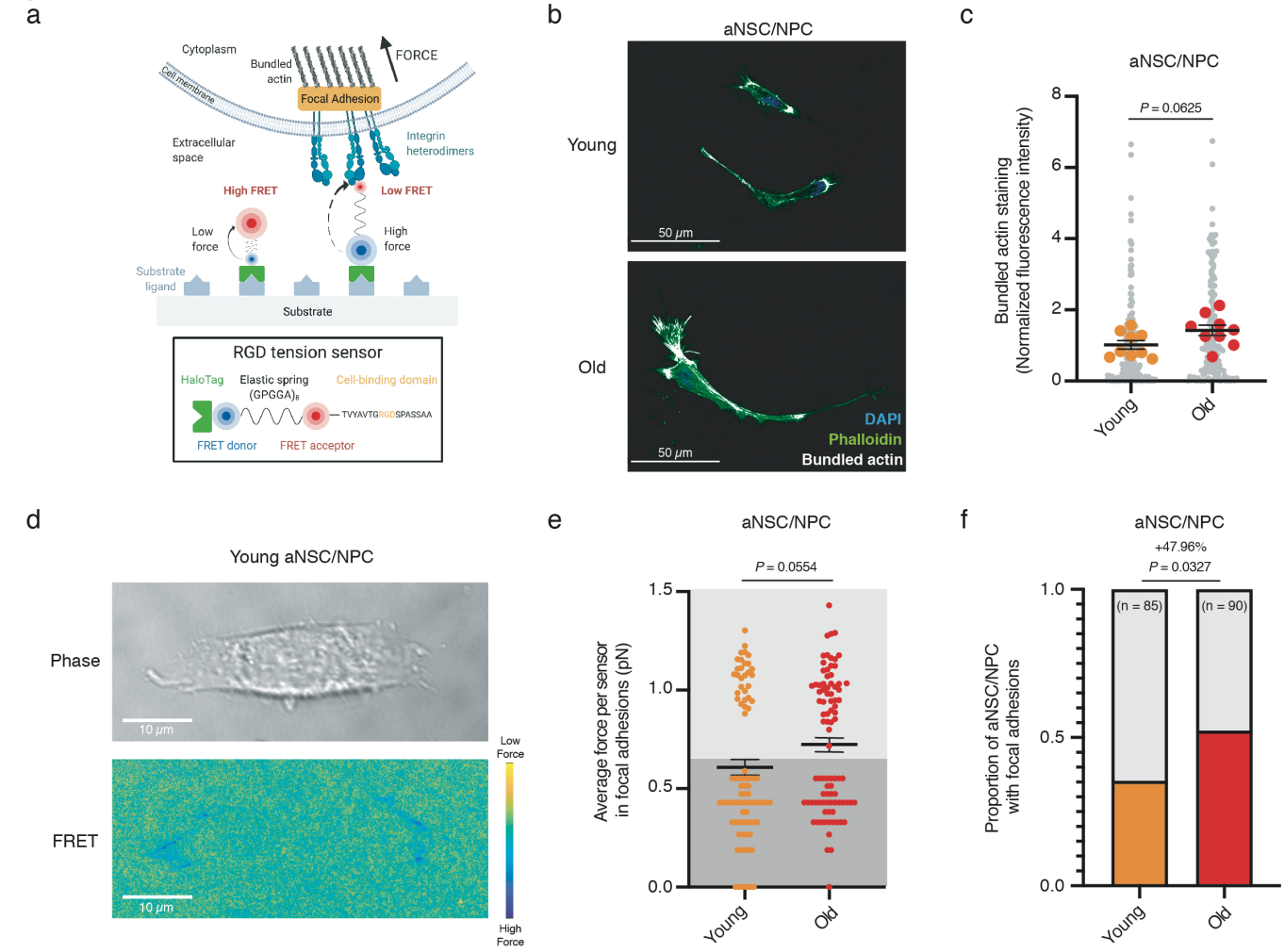
a
Cytoplasm
Bundled actin
FORCE
Cell membrane
Focal Adhesion
Extracellular space
Integrin heterodimers
High FRET
Low FRET
Low force
High force
Substrate ligand
Substrate
RGD tension sensor
HaloTag
Elastic spring (GPGGA)8
Cell-binding domain
TVYAVTGRGDSPASSAA
FRET donor
FRET acceptor
b
aNSC/NPC
Young
Old
50 μm
DAPI
Phalloidin
Bundled actin
c
aNSC/NPC
P = 0.0625
Bundled actin staining (Normalized fluorescence intensity)
Young
Old
d
Young aNSC/NPC
Phase
FRET
10 μm
Low Force
High Force
e
aNSC/NPC
P = 0.0554
Average force per sensor in focal adhesions (pN)
Young
Old
f
aNSC/NPC
+47.96%
P = 0.0327
(n = 85)
(n = 90)
Proportion of aNSC/NPC with focal adhesions
Young
Old

1407 **Figure 4: Aging increases the occurrence of force-producing focal adhesions in**

1408 **aNSCs/NPCs**

1409

1410 **a)** Diagram of RGD molecular tension sensor (adapted from previous work[55]). As cells adhere

1411 to the tension sensor-coated substrate, integrin heterodimers bind to the RGD cell-binding

1412 domain and exert force across a molecular spring, resulting in decreased FRET signal. RGD,

1413 peptide containing tripeptide Arg-Gly-Asp motif. FRET, Förster resonance energy transfer.

1414 **b)** Representative images of immunofluorescence staining of young (3-4 months) (top) and old

1415 (21-24 months) (bottom) cultured aNSCs/NPCs on Poly-D-Lysine. Blue, DAPI (nuclei);

1416 green, phalloidin (F-actin); white, high-intensity phalloidin mask (bundled actin). Scale bar,

1417 50 μm.

1418 **c)** Bundled actin fluorescence intensity in young (3-4 months) and old (21-24 months) cultured

1419 aNSCs/NPCs, normalized to the mean levels of the young condition. Each gray dot

1420 represents bundled actin levels in a single cell and each colored dot represents the average

1421 cellular bundled actin level per animal (n = 9 young male mice, and n = 9 old male mice)

1422 (combined over 3 experiments). Data are mean ± SEM. P-values were calculated using a

1423 two-tailed Mann-Whitney test comparing sample means between conditions.

1424 **d)** Representative image of a young (3 months) cultured aNSC/NPC seeded on RGD molecular

1425 tension sensors taken with phase contrast (top) and FRET donor/acceptor fluorescence

1426 wavelengths to generate a high-resolution traction map of FRET efficiency (bottom). The

1427 colored bar reflects the FRET efficiency, a measure of adhesion strength, where a low FRET

1428 efficiency indicates high force (blue color) and a high FRET efficiency indicates low force

1429 (yellow/green color). Scale bar, 10 μm.

1430 **e)** Average force per sensor (pN) in individual focal adhesions exhibited by young (3 months)
1431 and old (21 months) cultured aNSCs/NPCs determined using RGD molecular tension sensors
1432 (n = 85 young aNSCs/NPCs, and n = 90 old aNSCs/NPCs) (combined over 2 separate
1433 experiments). Shading delineates the bimodal populations of cells with active focal adhesions
1434 (light grey, each dot represents the average force sensor reading among focal adhesions for a
1435 single cell) or no detected focal adhesion (dark grey, each dot represents the average force
1436 sensor reading underneath the cell body). *P*-values were calculated using a two-tailed Mann-
1437 Whitney test.
1438 **f)** Fraction of young (3 months) and old (21 months) cultured aNSCs/NPCs exhibiting focal
1439 adhesion patterns as determined from RGD tension sensor experiments (combined over 2
1440 separate experiments). *P*-values were calculated using a combined Fisher's exact test.
1441
1442
1443
1444
1445
1446
1447
1448
1449
1450
1451

Figure 5

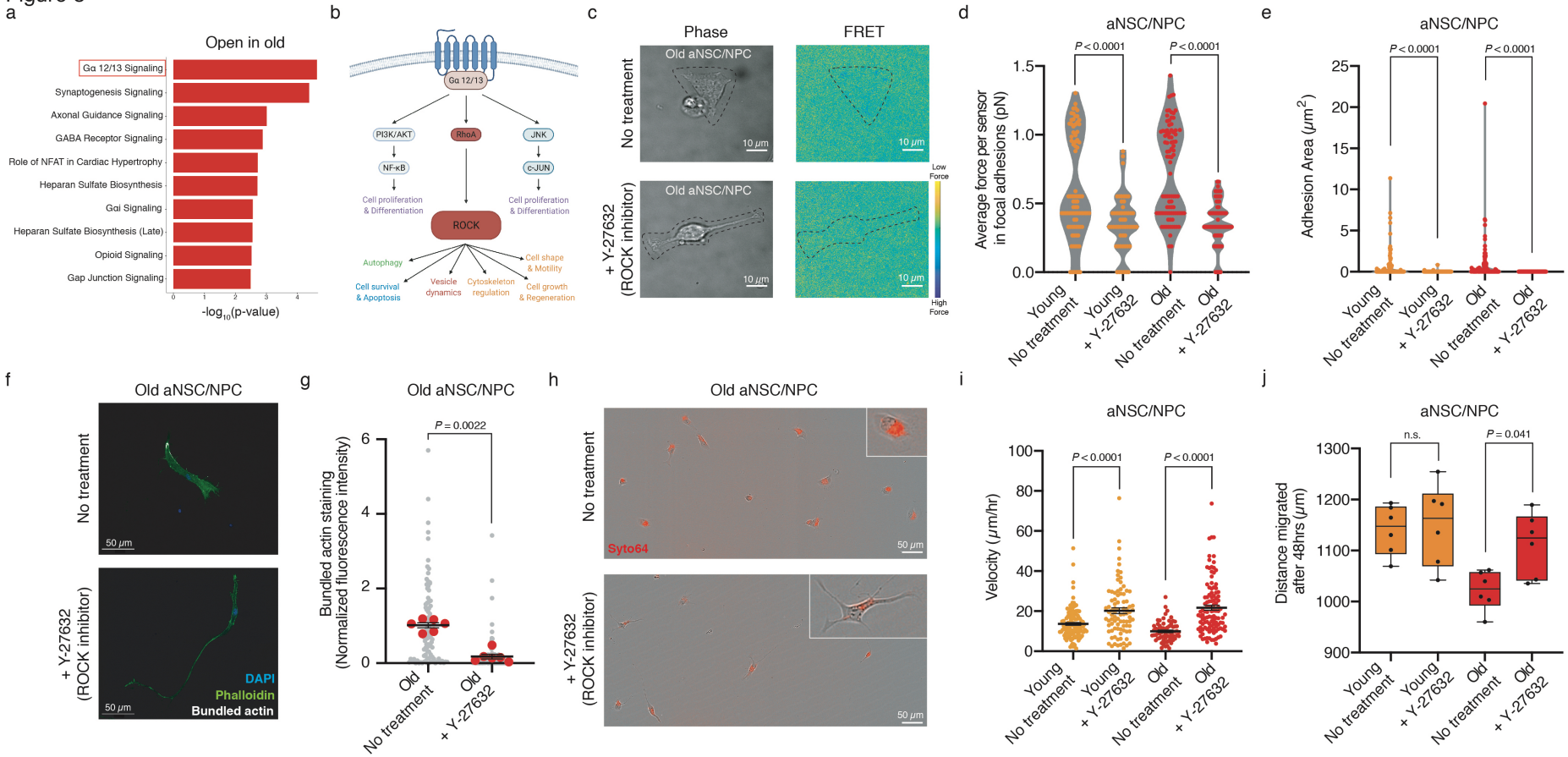
a
Open in old
Gα 12/13 Signaling
Synaptogenesis Signaling
Axonal Guidance Signaling
GABA Receptor Signaling
Role of NFAT in Cardiac Hypertrophy
Heparan Sulfate Biosynthesis
Gαi Signaling
Heparan Sulfate Biosynthesis (Late)
Opioid Signaling
Gap Junction Signaling
-log10(p-value)
b
Gα 12/13
PI3K/AKT
RhoA
JNK
NF-κB
c-JUN
Cell proliferation & Differentiation
Cell proliferation & Differentiation
ROCK
Autophagy
Cell survival & Apoptosis
Vesicle dynamics
Cytoskeleton regulation
Cell shape & Motility
Cell growth & Regeneration
c
Phase
FRET
No treatment
+ Y-27632 (ROCK inhibitor)
Old aNSC/NPC
Old aNSC/NPC
10 μm
Low Force
High Force
d
aNSC/NPC
P < 0.0001
P < 0.0001
Average force per sensor in focal adhesions (pN)
Young No treatment
Young + Y-27632
Old No treatment
Old + Y-27632
e
aNSC/NPC
P < 0.0001
P < 0.0001
Adhesion Area (μm2)
f
Old aNSC/NPC
No treatment
+ Y-27632 (ROCK inhibitor)
50 μm
DAPI
Phalloidin
Bundled actin
g
Old aNSC/NPC
P = 0.0022
Bundled actin staining (Normalized fluorescence intensity)
Old No treatment
Old + Y-27632
h
Old aNSC/NPC
No treatment
+ Y-27632 (ROCK inhibitor)
Syto64
50 μm
i
aNSC/NPC
P < 0.0001
P < 0.0001
Velocity (μm/hr)
Young No treatment
Young + Y-27632
Old No treatment
Old + Y-27632
j
aNSC/NPC
n.s.
P = 0.041
Distance migrated after 48hrs (μm)
Young No treatment
Young + Y-27632
Old No treatment
Old + Y-27632

1452 **Figure 5: Inhibition of ROCK boosts migration speed and eliminates focal adhesions in**
1453 **aNSCs/NPCs from aged brains**
1454
1455 **a)** Top 10 canonical pathways enriched for genes associated with differentially accessible peaks
1456 that open with age in freshly isolated aNSCs (FDR<0.05) generated by Ingenuity Pathway
1457 Analysis (IPA) and ranked by *P*-value. ATAC-seq peaks were annotated with their nearest
1458 gene using ChIPSeeker (v1.18.0) and *P*-values were calculated using Fisher's Exact Test by
1459 IPA.
1460 **b)** Diagram of the Gα 12/13 signaling pathway with selected targets including ROCK and
1461 downstream biological processes regulated by ROCK (adapted from the IPA canonical
1462 pathway diagram "Gα 12/13 Signaling" and previous work[86]). RhoA, Ras homolog family
1463 member A. ROCK, Rho-associated coiled-coiled kinase. PI3K, phosphoinositide 3-kinase.
1464 AKT, AKT serine/threonine kinase 1. NF-κB, Nuclear factor-kappa B. JNK, c-Jun N-
1465 terminal kinase.
1466 **c)** Representative images of old (21 months) cultured aNSCs/NPCs treated with H_2O vehicle
1467 (top) or with 10 μM Y-27632 (bottom) seeded on RGD molecular tension sensors taken with
1468 phase contrast (left) and FRET donor/acceptor fluorescence wavelengths to generate a high-
1469 resolution traction map of FRET efficiency (right). A low FRET efficiency indicates high
1470 force (blue color) and a high FRET efficiency indicates low force (yellow/green color). Black
1471 dotted lines around the adhered cell bodies were generated using phase contrast images and
1472 overlaid onto FRET images. Scale bar, 10 μm.
1473 **d)** Truncated violin plot of average force per sensor (pN) in individual focal adhesions exhibited
1474 by young (3 months) and old (21 months) cultured aNSCs/NPCs treated with H_2O vehicle or

1475 with 10 μM Y-27632 determined using RGD molecular tension sensors (*n* = 85 young
1476 aNSCs/NPCs, *n* = 54 young aNSCs/NPCs + 10 μM Y-27632, *n* = 90 old aNSCs/NPCs, and *n*
1477 = 74 old aNSCs/NPCs +10 μM Y-27632) (combined over 2 separate experiments). For cells
1478 exhibiting focal adhesion patterns, each dot represents the average force sensor reading
1479 among focal adhesions for a single cell. For cells without any focal adhesions, each dot
1480 represents the average force sensor reading underneath the cell body. *P*-values were
1481 calculated using a two-tailed Mann-Whitney test.

1482 **e)** Truncated violin plot of adhesion area under focal adhesions of young (3 months) and old (21
1483 months) aNSCs/NPCs treated with H_2O vehicle or with 10 μM Y-27632 determined using
1484 RGD molecular tension sensors (*n* = 85 young aNSCs/NPCs, *n* = 54 young aNSCs/NPCs +
1485 10 μM Y-27632, *n* = 90 old aNSCs/NPCs, and *n* = 74 old aNSCs/NPCs +10 μM Y-27632)
1486 (combined over 2 separate experiments). Each dot represents the adhesion area of force-
1487 producing focal adhesions for a single cell. *P*-values were calculated using a two-tailed
1488 Mann-Whitney test.

1489 **f)** Representative images of immunofluorescence staining of an old (21-23 months old)
1490 aNSC/NPC treated with H_2O vehicle (top) or with 10 μM Y-27632 (bottom) cultured on
1491 Poly-D-Lysine. Blue, DAPI (nuclei); green, phalloidin (F-actin); white, high-intensity
1492 phalloidin mask (bundled actin). Scale bar, 50 μm.

1493 **g)** Fluorescence intensity of bundled actin in old (21-23 months) aNSCs/NPCs treated with H_2O
1494 vehicle or with 10 μM Y-27632 cultured on Poly-D-Lysine, normalized to the mean levels of
1495 the untreated condition. Each gray dot represents bundled actin levels in a single cell and
1496 each colored dot represents the average cellular bundled actin level per animal (*n* = 6 old
1497 cultures for both untreated and treated conditions) (combined over 2 experiments). Data are

1498 mean ± SEM. *P*-values were calculated using a two-tailed Mann-Whitney test comparing
1499 sample means between conditions.

1500 **h)** Representative images of old (21-24 months) cultured aNSCs/NPCs 12 hours after sorting
1501 onto Poly-D-Lysine-coated migration plates treated with H_2O vehicle (top) or 10μM Y-
1502 27632 (bottom). Images were taken with the Incucyte S3 system with phase contrast and RFP
1503 imaging overlaid. Live cells were stained with Syto64, a cell-permeant red fluorescent
1504 nucleic acid stain, for migration tracking. Outlined inset (top-right) displays a representative
1505 magnified cell. Scale bar, 50 μm.

1506 **i)** Migration speed of young (3-4 months) and old (21-24 months) aNSCs/NPCs cultured on
1507 Poly-D-Lysine treated with H_2O vehicle or with 10 μM Y-27632. Each dot represents the
1508 average velocity of a single cell over a 20-hour period (n = 9 young control cultures, n = 9
1509 young treatment cultures, n = 7 old control cultures, n = 9 old treated cultures) (combined
1510 over 3 experiments). Data are mean ± SEM. *P*-values were calculated using a two-tailed
1511 Mann-Whitney test.

1512 **j)** Distance migrated through Matrigel after 48 hours by young (3-4 months) and old (21-23
1513 months) cultured aNSCs/NPCs treated with H_2O vehicle or with 10 μM Y-27632. Each dot
1514 represents the distance migrated by a single biological replicate after 48 hours (n = 6 young
1515 cultures for treated and untreated conditions, n = 6 old cultures for treated and untreated
1516 conditions) (combined over two experiments). For each biological replicate, 1-4 technical
1517 replicates were evaluated, and migration distance was averaged. *P*-values were calculated
1518 using a two-tailed Mann-Whitney test.